# Overview: Precipitation Characteristics and Sensitivities to Environmental Conditions during GoAmazon2014/5 and ACRIDICON-CHUVA

Luiz A. T. Machado[1], Alan J. P. Calheiros[1], Thiago Biscaro[1], Scott Giangrande[2], Maria A. F. Silva Dias[3], Micael A. Cecchini[3], Rachel Albrecht[3], Meinrat O. Andreae[4,14], Wagner F. Araujo[1], Paulo Artaxo[5], Stephan Bormann[4], Ramon Braga[1], Casey Burleyson[6], Cristiano W. Eichholz[1], Jiwen Fan[6], Zhe Feng[6], Gilberto F. Fisch[8], Michael P. Jensen[2], Scot T. Martin[7], Ulrich Pöschl[4], Christopher Pöhlker[4], Mira L. Pöhlker[4] Jean-François Ribaud[1], Daniel Rosenfeld[9], Jaci M. B. Saraiva[10], Courtney Schumacher[11], Ryan Thalman[12] David Walter[4] and Manfred Wendisch[13]

[1]National Institute for Space Research (INPE), Sao José dos Campos, Brazil
[2]Brookhaven National Laboratory, Upton, New York, USA
[3]Institute of Astronomy, Geophysics, and Atmospheric Sciences, University of São Paulo, Brazil
[4]Max Planck Institute for Chemistry, Mainz, Germany
[5]Institute of Physics, University of São Paulo, São Paulo, Brazil
[6]Pacific Northwest National Laboratory, Richland, WA
[7]Harvard University, Cambridge, Massachusetts, USA
[8]Department of Aerospace Science and technology
[9]Hebrew University of Jerusalem, Israel
[10]Amazon Protection System (SIPAM), Manaus, Brazil
[11]Texas A&M University, College Station, Texas, USA
[12]Snow College, USA
[13]Leipzig Institute for Meteorology, Leipzig University, Leipzig, Germany
[14]Scripps Institution of Oceanography, University of California San Diego, CA 92037, USA

*Correspondence to*: Luiz A. T. Machado (luiz.machado@inpe.br)

**Abstract.** This study provides an overview of precipitation processes and their sensitivities to environmental conditions in the Central Amazon Basin near Manaus during the GoAmazon2014/5 and ACRIDICON-CHUVA experiments. This study takes advantage of the numerous measurement platforms and instrument systems operating during both campaigns to sample cloud structure and environmental conditions during 2014 and 2015; the rainfall variability among seasons, aerosol loading, land surface type, and topography have been carefully characterized using these data. Differences between the wet and dry seasons were examined from a variety of perspectives. The rainfall rates distribution, total amount of rainfall, and raindrop size distribution (the mass-weighted mean diameter) were quantified over both seasons. The dry season generally exhibited higher rainfall rates than the wet season and included more intense rainfall periods. However, the cumulative rainfall during the wet season was four times greater than that during the total dry season rainfall, as shown in the total rainfall accumulation data.

The typical size and life cycle of Amazon cloud clusters (observed by satellite) and rain cells (observed by radar) were examined, as were differences in these systems between the seasons. Moreover, monthly mean thermodynamic and dynamic variables were analysed using radiosondes to elucidate the differences in rainfall characteristics during the wet and dry seasons. The sensitivity of rainfall to atmospheric aerosol loading was discussed with regard to mass-weighted mean diameter and rain rate. This topic was evaluated only during the wet season due to the insignificant statistics of rainfall events for different aerosol loading ranges and the low frequency of precipitation events during the dry season. The impacts of aerosols on cloud droplet diameter varied based on droplet size. For the wet season, we observed no dependence between land surface type and rain rate. However, during the dry season, urban areas exhibited the largest rainfall rate tail distribution, and deforested regions exhibited the lowest mean rainfall rate. Airplane measurements were taken to characterize and contrast cloud microphysical properties and processes over forested and deforested regions. Vertical motion was not correlated with cloud droplet sizes, but cloud droplet concentration correlated linearly with vertical motion. Clouds over forested areas contained larger droplets than clouds over pastures at all altitudes. Finally, the connections between topography and rain rate were evaluated, with higher rainfall rates identified at higher elevations during the dry season.

## 1. Introduction

### 1.1 - The Amazon Forest Climate

The Amazon Forest spans more than 3,000 km in the east-west direction and approximately 2,000 km from north to south. It crosses the equator but is primarily located in the Southern Hemisphere and encompasses both equatorial and tropical climates. The northern expanse of the Amazon Basin is influenced by the tropical Atlantic Ocean, while the western edge is dominated by the Andes Mountains, which rise more than 4,000 m above sea level in the tropical and equatorial regions.

Cavalcanti et al. (2009) have provided a detailed picture of weather and climate in Brazil, particularly in the Amazon. The dominant large-scale features in the Amazon are the lack of major temperature gradients and the absence of baroclinic weather systems. However, these features do not mean that there is a lack of convective organization. The main synoptic systems that approach the region and alter weather conditions are: a) the Intertropical Convergence Zone, mostly affecting the northern half of the Amazon; b) the easterly waves coming from the tropical Atlantic (Diedhiou et al., 2010); c) the upper tropospheric cyclonic vortices originating on the eastern coast of northeast Brazil and the associated upper air Bolivian High (Silva Dias et al., 1983 and Kousky and Gan, 1981); d) the South Atlantic Convergence Zone, which affects the southern half of the Amazon and has a major effect on Amazonian convective activity as a whole (Rickenbach et al., 2002); and e) the northward propagation of convective clouds (Siqueira and Machado, 2004) and the remnants of mid-latitude cold frontal systems that may propagate northward, sometimes beyond the equator, resulting in so called “friagem” events (Marengo et al., 1997). Within the Basin, convection is often organized into squall lines (Cohen et al., 1995) that frequently occur as large systems originating at the northern coast and are triggered by local sea breeze circulation (Greco et al., 1994). Some of these squall lines propagate to Central Amazonas, dissipating during the night and reactivating the next day by diurnal heating.

Climate controls on Amazon Basin rainfall come from El Niño/La Niña episodes, which are defined by tropical Pacific Ocean sea surface temperatures (SSTs) and tropical Atlantic SSTs (Marengo et al., 2013, 2016). Warm tropical Atlantic SSTs are associated with drought conditions in the Amazon region. During El Niño episodes, most of the Amazon Basin experiences below-average rainfall, while during La Niña cases, the basin experiences above-average rainfall. The convective activity in most of the Amazon Basin is part of the South American Monsoon System (SAMS), which is associated with distinct wet and dry seasons (Silva Dias and Carvalho, 2016).

Horel et al. (1989) used satellite downward longwave radiation to characterize seasonal variations in the Amazon and found that the region experiences typical wet and dry seasons each year, with two transition periods in between them. Machado et al. (2004) has defined the driest month and the duration of the dry season regionally within the Amazon Basin. The dry season varies from only one month in the northwest to 3-4 months in southeastern Amazonas. For the Central Amazonas region, July, August and September are typically the driest months. Convection in Amazonas is more intense during the dry to wet transition season, during which thunderstorms exhibit more lightning activity (Albrecht et al., 2011) and are more sensitive to aerosol loading and topography (Gonçalves and Machado, 2015). The transition from the dry to wet season is influenced by complex interactions between smoke-derived aerosols and deep convective clouds (Albrecht et al., 2011). Although the seasonal variability in the average convective available potential energy (CAPE) is small, the tail of the CAPE's seasonal distribution (computed as the surface parcel) exhibits relatively higher values during the dry to wet season transition than during the wet season (Williams et al., 2002). During the dry season, the aerosols produced by biomass burning in central South America impact a larger area, reaching the tropical Pacific, subtropical South America and South Atlantic (Andreae et al., 2001; Freitas et al., 2005, 2016; Camponogara et al., 2014).

While the Amazonas region exhibits strong seasonal variations in atmospheric circulation and related precipitation patterns, the diurnal cycle is typically the same throughout the year. Most of the region has an afternoon peak of convective activity; however, selected areas experience quite intense nocturnal systems and more pronounced seasonality (Saraiva et al., 2016). The diurnal convection cycle is strongly linked to underlying surface features (Machado et al., 2004; Silva Dias et al., 2002), including its topography (Laurent et al., 2002), deforestation (Saad et al., 2010) and large rivers (Dos Santos et al., 2014; Silva Dias et al., 2004). Additionally, large rivers impact the evolution of rainfall through the convergence of river breezes with ambient air flow (Fitzjarrald et al., 2008). Adams et al. (2016) have shown that one central problem of the climate model related to the Amazon's diurnal convection and rainfall variability is the transition from shallow-to-deep convection, which occurs on a time scale of approximately three hours.

The evolution of the boundary layer in the Amazon region has been studied during intensive field observations conducted in different sub-regions in the Amazon Basin, including The Amazon Boundary Layer Experiment (ABLE 2A, 2B, see Harris et al., 1988, 1990), the Anglo-Brazilian Amazonian Climate Observation Study (ABRACOS, see Gash et al., 1996), the Large-Scale Biosphere Atmosphere experiment in Amazonia (LBA, see Silva Dias et al., 2002), the Cloud Processes of the Main Precipitation Systems in Brazil: A Contribution to Cloud-Resolving Modelling and to the Global Precipitation Measurement (CHUVA, Machado et al., 2014) combined with ACRIDICON (Aerosol, Cloud, Precipitation, and Radiation Interactions and

Dynamics of Convective Cloud Systems, Wendisch et al., 2016), and the Green Ocean Amazon GoAmazon2014/5 (Martin et al., 2017). Fisch et al. (2004) have indicated that the evolution of the boundary layer in the Amazon is linked to land cover and soil moisture, with a deeper mixed layer in the dry season over deforested areas and a shallower mixed layer over forested areas. During the wet season, there are small differences between the evolution of the mixed layer over forested and deforested regions.

During the dry season, the lower atmosphere is polluted by high aerosol concentrations caused by both biomass burning and prolonged aerosol suspension associated with reduced precipitation (Artaxo et al., 2002 and Martin et al., 2010). During the wet season, the atmosphere is mostly clean and convective, and the landscape is referred to as the Green Ocean (Roberts et al., 2001; Williams et al., 2002 and Andreae et al., 2004) because the convection there resembles storms over blue oceans, where the warm phase in clouds generally produces rain. Large urban areas, however, introduce perturbations into the pristine air (Martin et al., 2016, 2017).

The complex physico-chemical interactions observed in the Amazon Basin include rainfall formation processes; diurnal, seasonal, and interannual cycles; the spatial organization of clouds; the mechanisms controlling cloud condensation nuclei (CCN); and the interactions between the vegetation, atmospheric boundary layer, clouds and upper troposphere. These processes are all in perfect sync, resulting in a stable equilibrium climate that produces rainfall equivalent to 2.3 metres throughout the 6.1 million square kilometres of the Amazon Basin, or the equivalent of an average 27 trillion metric tons of rainfall each year. However, this amazing, complex mechanism can be modified by human activities. A recent study illustrates and quantifies (Fu et al., 2013) how this stable environment can be disturbed and the point of equilibrium shifted far from the one that produces abundant fresh water, keeps the forest alive and plays a primary role in controlling global atmospheric circulation and energy distribution.

### 1.2 Knowledge about Cloud Process in the Amazon Acquired during Field Campaigns

The most recent GoAmazon2014/5, and CHUVA-ACRIDICON measurement campaigns established a comprehensive dataset to elucidate the complex aerosol-cloud-precipitation interactions within the Amazon Basin. The GoAmazon observations, collected over two years, have delivered a wealth of data on aerosol-cloud-precipitation (ACP) interactions (Martin et al., 2016). During the two intensive operation periods (IOPs) conducted during the wet and dry seasons, additional airplane data were collected by the IARA (Intensive Airborne Research in Amazonas), Martin et al. (2017) and the ACRIDICON campaign (Wendisch et al., 2016). The data collected under the umbrella of the GoAmazon campaign also include the CHUVA Project (Machado et al., 2014) and several other initiatives, which have compiled the most complete dataset in Amazonas associated with atmospheric chemical and physical interactions. GoAmazon2014/5 data were collected in the environs of Manaus city, the capital of Amazonas State. Manaus is a city of around two million people located in the middle of Central Amazonas and serves as a natural laboratory from which to explore the urban pollution effects on Amazonas's background environment.

Recent work by Gerken et al. (2015) has shown strong enhancement of ozone concentrations close to the surface during storm downdrafts in the central Amazon and suggests that storm downdrafts bringing higher ozone concentrations from middle-higher altitudes play an important role in enhancing ozone concentrations. The same effect was found by Betts et al. (2002) in the southwest Amazon during LBA. Wang et al. (2016) used airplane (G1) data to describe the mechanism by which aerosol concentrations are maintained in the pristine Amazonian boundary layer. Aerosol losses via precipitation scavenging at the surface are replaced by storm downdraft fluxes that bring high concentrations of nanosized particles from the upper atmosphere during precipitation events. These nanoparticles combine with the oxidation products of VOCs (Volatile Organic Compounds) to form CCN at the surface and assist in the formation of clouds. Measurements by the G1 and by HALO (High Altitude and Long-Range Research Aircraft) show a very high concentration of nanoparticles in the upper troposphere, with concentrations up to 65,000 particles per $cm^3$ (Andreae et al., 2017).

Aerosol particles influence cloud formation. Cecchini et al. (2016) have highlighted the effects of the Manaus aerosol pollution plume on cloud droplet size distribution during the wet season when only a small sensitivity would be expected. They describe the significant influence of the Manaus pollution plume in reducing the size and increasing the number of cloud droplets as well as the total liquid water content. The ACRIDICON-CHUVA campaign collected in situ data during 14 research flights using the HALO research aircraft (Wendisch et al., 2016). The high number of flight hours inside growing cumulus clouds allowed a sensitivity analysis of aerosol concentrations and of the thermodynamic effects of such concentrations in the warm phase of cumulus clouds. Cecchini et al. (2017a) have also demonstrated that a 100% increase in aerosol concentrations led to an 84% increase in the concentration of droplets, but the same relative increase in vertical velocity corresponded only to a 43% change. Braga et al. (2017) have compared HALO microphysical probe measurements of cloud droplet concentrations with a parameterization based on CCN and updraft at the cloud base. Jäkel et al. (2017) have presented a new methodology to retrieve the vertical distribution of the hydrometeor phase using cloud-side reflected solar radiation measurements and have discussed the mixed phase layer as a function of aerosol loading. Giangrande et al. (2016) have presented the statistical behaviour of vertical cloud motions as a function of season, instability and convective inhibition. Burleyson et al. (2016) have discussed the diurnal cycle and spatial variability of deep convection among the different GoAmazon sites. Giangrande et al. (2017) have also presented an overview of cloud, thermodynamics, and radiation interactions.

Preceding GoAmazon2014/5, ABLE-2 and LBA collected cloud and rainfall data used to understand rainfall variability and its interaction with surface vegetation, topography and aerosols in the Amazon. The ABLE-2 project consisted of two expeditions: the first in the Amazonian dry season (ABLE-2A) during July August 1985 and the second in the wet season (ABLE-2B) during April-May 1987 (Harriss et al., 1988, 1990). Greco et al. (1990) have described the rainfall and kinematics of the central Amazon using GOES (Geostationary Operational Environmental Satellite) imagery, revealing the importance of tropical squall lines on the rainfall regime of the Amazon. Some years later, Garstang et al. (1994), Greco et al. (1994) and Cohen et al. (1995) provided a detailed description of tropical squall lines in the region. The TRMM-LBA campaign was designed to calibrate the TRMM (Tropical Rainfall Measuring Mission) satellite. The observations were conducted in southern Amazonas along the arc of deforestation during the wet season. Several studies contributed to our current understanding of

rainfall variability at different scales. Machado et al. (2002) discussed the complex diurnal cycle interaction at a synoptic scale, while Laurent et al. (2002) examined the mesoscale convective system initiation and propagation; and Rickenbach et al. (2004) showed the importance of nocturnal clouds in rainfall in southwestern Amazonas. Silva Dias et al. (2002), Petersen et al. (2001), and Cifelli et al. (2002) have all published findings using TRMM-LBA data to describe the microphysical properties of the rainfall field, cloud processes, and biospheric interactions in this region. In addition, different rainfall features have been detected associated with wind regimes; in particular, easterlies and westerlies in the southern Amazon have been associated with breaks and active phases of the South American Monsoon System (Silva Dias and Carvalho, 2016, Rickenbach et al. 2002). In the northwestern Amazon, northerlies and southerlies are associated with more stratiform and convective systems, respectively (Saraiva et al. 2016).

Other studies discuss the rainfall regime in Amazonas State. For example, Tanaka et al. (2014) have described the influence of the river and the city of Manaus in the diurnal cycle of rainfall using rain gauge data. Dos Santos et al. (2014) used satellite rainfall products to define the features associated with river breezes associated with the Negro, Solimões and Amazon Rivers. Fitzgerald et al. (2008) have described the effect of the Tapajos River on rainfall, and Silva Dias et al. (2004) have shown how wind structure favours cloud formation on the upwind side of the Tapajós River during daytime. Negri et al. (2000) used passive microwave radiances to construct a 10-year climate related to the Amazonas's rainfall patterns. Saraiva et al. (2016) have described the general statistics related to Amazonas rainfall using the meteorological S-band radar operational network and have discussed the diurnal cycle as well as the relationship between reflectivity and the cloud electrification process.

All of these studies have contributed to the establishment of our basic knowledge about the rainfall statistics and related processes in Amazonas; they have provided a new perspective for research in Amazonas and have elucidated several aspects of ACP interactions. The studies associated with field campaigns covered specific seasons (normally the wet season) or resulted from sparse rain gauge or indirect measurement data with low spatial and temporal resolutions. In GoAmazon2014/5, the extensive rainfall dataset collected using the S, X, and W band radars; airplanes; disdrometers vertical pointing radar; rain gauges; microwave radiometers; ceilometers; and LIDAR provides a comprehensive view of the main variables and characteristics of precipitation in the central Amazon.

Giangrande et al. (2017) present an overview of clouds aspect that primarily focuses on the diurnal cycle and its impact on the radiative and thermodynamics effects of clouds. This study presents an overview of the rainfall characteristics and sensitivities to vegetation, topography, and aerosol particles and evaluates the seasonal variability of these factors. The main goal is to discuss the sensitivities of the primary processes controlling rainfall over the central Amazon using a relatively long time series (2014-2015) of data based on a comprehensive dataset collected during GoAmazon2014/5 and complemented by aircraft measurements made during ACRIDICON-CHUVA.

Section 2 describes the data and methodology employed in the study. Section 3 presents the results and discussions of the seasonal rainfall characteristics and sensitivities to aerosol, vegetation and topography; and Section 4 summarizes the major findings.

## 2. Data and Methodology

Several instruments were employed in this study. This section describes the instruments and the data processing procedures. Figures 1 and 2 in the Martin et al. (2016) study show the GoAmazon site locations and the flight tracks of the G1 aircraft. Wendisch et al. (2016) show the flight tracks (Figure 6) of the HALO aircraft during the ACRIDICON-CHUVA campaign.

A laser precipitation disdrometer (PARSIVEL, see Löffler-Mang and Joss, 2000) measures the size and terminal velocity of hydrometeors that pass through the detection area sampled by a laser beam (54 $cm^2$) over a specific time interval. Two different PARSIVEL disdrometers were used during the entire campaign: one during the CHUVA Project from January to September 2014 and another during ARM (Atmospheric Radiation Measurement) from September 2014 to October 2015. Raindrops larger than 5 mm were eliminated from the dataset to best match the co-located rain gauge accumulated rainfall; and a complementary filter was applied as described by Giangrande et al. (2016). The drop size distribution (DSD) and all respective rainfall rates (RR, in mm $h^{-1}$) and mass-weighted mean diameters ($D_m$, in mm) were obtained in 5-minute intervals for periods where RR $\geq$ 0.5 mm $h^{-1}$, as suggested by Tokay et al. (2013).

The Doppler radar S-band dataset consists of retrievals from the Manaus radar operated by the Amazon Protection System (SIPAM). The reflectivity and RR fields were computed using the 2.5 km SIPAM Manaus S-band Constant Altitude Plan Position Indicator (CAPPI) for each radar volume at 10-minute intervals. The corrected radar reflectivity for each volume was interpolated to a fixed grid on which the rainfall products were generated. Specific procedures were applied to the dataset to compute RRs from reflectivity, reduce noise, and improve data quality. First, RRs were computed using a Z-R relationship adjusted to the region using 2014 wet season impact disdrometer data: $Z=174.8R^{1.56}$. This is a fixed Z-R relationship for convective and stratiform clouds and for both the wet and dry seasons. Therefore, the total rainfall estimated should be considered a reference by which to study the differences among the topography and vegetation classes and not as an absolute, precise rainfall amount. The maximum and minimum RRs considered were 160 mm $h^{-1}$ and 0.5 mm $h^{-1}$, respectively. The RR was not computed when the radar beam had less than 10% quality reflectivity values (non-null reflectivity). Finally, a range filter was applied to remove pixels closer than 10 km and farther than 135 km from the radar.

The Doppler radar X-band dual-polarization dataset was obtained by the mobile Meteor 50DX Selex radar during the CHUVA Project (Schneebeli et al., 2012). The radar data underwent three main processing steps, including differential phase shift (PhiDP) filtering and specific differential phase (KDP) derivation, differential reflectivity (ZDR) offset correction, and horizontal reflectivity (Zh) and ZDR attenuation correction. The uncorrected raw differential phase shift had a noisy signal that required filtering and smoothing before its range derivative (KDP) could be calculated. Several methods were available for use, such as a moving average, median filters, and linear programming approaches. In this study, we used the finite impulse response (FIR) filter based on Hubbert and Bringi (1995). Once the filtered PhiDP profile was obtained, KDP was calculated using a least squares linear fit. To verify and calibrate the accuracy of the differential reflectivity measurement, a vertical pointing, rotating scan (also known as “bird-bath” scan) was incorporated into the X-band scan strategy. During light precipitation and in the absence of strong winds, the vertical and horizontal return signals of a vertically oriented beam should

be the same. Differences between the horizontal and vertical channels may appear due to poor calibration between the channels, random effects, beam-filling, or side-lobe clutter contamination, among other factors (Gorgucci et al., 1999). Although standard calibration was performed, careful examination of the ZDR behaviour before and after the calibration was necessary. We selected all of the observations with no radar gates higher than 30 dBZ below 2 km and analysed the overall ZDR values and temporal changes in the mean value. A persistent, positive ZDR offset (approximately 0.5 dB) was found and applied to the data. After these steps, we applied an attenuation correction. X-band radars are more prone to signal attenuation due to rain than C- and S-band radars. It is therefore mandatory to correct the signal for attenuation prior to any analysis using reflectivity data, if such a correction is possible (Schneebeli et al., 2012). With a dual-polarization system, one can use the differential phase shift to calculate the attenuation due to rain. We applied the ZPHI method (Testud et al., 2000) to the entire dataset where dual-polarization moments were available. The corrected Zh and ZDR values were then ready to be used as inputs for rainfall analyses or hydrometeor classification studies.

The cloud droplet size distributions were derived from the HALO measurements using a cloud droplet probe (CDP, Lance et al., 2010; Molleker et al., 2014 and Wendisch and Brenguier, 2013). This instrument measures the droplet size distribution within the size range of 3 µm to 50 µm based on the hydrometeor's forward scattering properties. The DSD is sorted into 15 size bins for each measurement cycle. The probe was operated at a 1 Hz frequency. The major sources of uncertainty for the instrument are as follows (Weigel et al., 2016): (a) uncertainty in the cross-section area (0.278 $mm^2$ +/- 15%), (b) the relatively small sample volume (cross-sectional area multiplied by aircraft speed), and (c) counting statistics for each size bin. As noted by Molleker et al. (2014), the CDP uncertainty is approximately 10%. Braga et al. (2017) performed an comparison between the CDP and the other HALO cloud probes and concluded that they agree within instrumental uncertainties. The vertical wind component (w) was measured by the Basic HALO Measurement and Sensor System (BAHAMAS) located at the nose of the aircraft (Wendisch et al., 2016) and calibrated according to Mallaun et al. (2015). The uncertainty in w is approximately 0.3 $m\ s^{-1}$.

Using the disdrometer or the CDP, the mass-weighted mean diameter ($D_m$) was computed as the ratio between the fourth and third moments (liquid water content) of the DSD (see Bringi et al., 2002 for a detailed description). For every five minutes of a continuous rainfall event (defined as $RR \geq 0.5\ mm\ h^{-1}$), the moments were computed using a parameterization derived by Tokay and Short (1996).

A condensation particle counter (CPC, TSI 3010) in the Aerosol Observing system instruments from ARM measured the concentration of individual aerosol particles at 10 m above ground level at the T3 site (main GoAmazon site at Manacapuru, see Martin et al., 2016 for a detailed description). The data were averaged to five-minute intervals covering the period from January 2014 to March 2015 (Thalman et al., 2017). Background or polluted conditions were defined based on the specific CPC distribution for each season by the threshold value associated with the 33% and 66% percentile, respectively, for the dry and wet seasons. The threshold values and details are presented in the relevant sections below.

The total concentration of individual cloud condensation nuclei particles ($N_{CCN}(S)$) was measured with a continuous-flow stream wise thermal-gradient CCN counter (model CCN-200, DMT, Longmont, CO, USA) (Rose et al., 2008). The measured

aerosol was sampled by the HALO aerosol submicrometer inlet (HASI). Particles with a critical supersaturation (S=0.52 ± 0.05%) were activated and formed water droplets. Water droplets with a diameter ≥ 1 μm were detected by an optical particle counter. Details about the measurement mode can be found in Andreae et al. (2017). The error in supersaturation resulted from the calibration uncertainty, as described by M. Pöhlker et al. (2016); it is estimated to be in the range of 10%.

This study considers the wet and dry seasons as the months of January to March and August to October, respectively. Some instruments operated only during the two GoAmazon2014/5 IOPs: IOP1 during the wet season, and IOP2 during the dry season. IOP1 corresponds to February to March and IOP2 to 15 September to 15 October. The S-band radar data are available for both years (2014 and 2015), while the X-band operated only in the 2014 IOPs.

Thermodynamic parameters such as CAPE, Convective Inhibition Energy (CINE), Precipitable Water Vapour (PWV), Lifting Condensation Level (LCL) and bulk shear were computed using the T3 radiosondes at 00, 06, 12 and 18 UTC for 2014. The thermodynamic parameters were computed using temperature and humidity at the surface. Bulk shear is defined as the difference between the average surface-6 km wind velocity and the surface-500 m wind velocity.

## 3. Results and Discussion

This section first discusses the rainfall characteristics and variability by comparing the wet and dry seasons to establish the primary differences between seasons. Section 3.2 discusses the sensitivity analyses relative to aerosols, vegetation and topography.

### 3.1 Rainfall Seasonal Variability

Seasonal variability was analysed from different perspectives, including general patterns, regional differences, satellite (clouds) and radar (rainfall) observation characteristics, DSD, rainfall vertical profile, and hydrometeor populations.

#### 3.1.1 General Precipitation and Thermodynamic Patterns.

Amazonas has a distinct seasonal variability with distinct wet and dry seasons. The length and start date of the wet season depends on the location within the Amazon Basin. The mean monthly rainfall (2014-2015) was 369 mm for the wet season (considering a month of 30 days) and 87 mm for the dry season. These numbers show the large difference expected between the two seasons. However, the RR (considering only when raining) also exhibited seasonal differences. The mean RR (computed in 5 minutes intervals) for the wet season was 7.7 mm $h^{-1}$, while that for the dry season was 9.4 mm $h^{-1}$. Therefore, although approximately 4 times less accumulated rainfall was recorded during the dry season than the wet season, the average rainfall event during the dry season produced a greater amount of rain. Figure 1 reveals this feature, where the relative rainfall rate distribution for the wet season shows higher relative frequency for RR < 20 mm $h^{-1}$ than that of the dry season. On the other hand, the dry season shows higher relative frequency for RR> 20 mm $h^{-1}$. There was only one event during the wet season in which a record RR of approximately 100 mm $h^{-1}$ was recorded within a few minutes. The relative intensity of dry season

rainfall events is more pronounced than that of events during the wet season. This distinctive feature has important consequences for the microphysical and macrophysical structures of clouds. The main reason for this difference is associated with instability and cloud cover. Figure 2 presents monthly box plots for the thermodynamics variables, with the lower (Q1) and upper (Q3) bounds representing the 25 and 75 percentiles. The whiskers are defined by Q1 - 1.5 * IQR (lower) and Q1 + 1.5 * IQR (upper); IQR is the interquartile range (Q3-Q1).

Figure 2A shows the CAPE distribution for the wet and dry seasons in 2014. The dry season has a larger CAPE than the wet season, and the frequency with which the CAPE exceeds 2000 J $kg^{-1}$ is higher during the dry season. The wet season has typical monsoonal rainfall, with widespread moderate rain, in contrast to the more isolated and intense rainfall events that occur during the dry season. Zhuang et al.'s (2017) study of shallow-to-deep convection transition in Amazonas found similar results.

This characteristic of rainfall events where a higher RR occurs during dry season rainfall events is explained by the seasonal differences in the thermodynamic parameters. Figure 2 highlights some of these important differences. The dry season has a larger CAPE, higher CINE, less available water vapour, a higher cloud base, and higher shear than the wet season. The CAPE increases from March to September; and the largest tail distributions occur at the end of the year when humidity increases and cloud base decreases. During the dry season, only regions with strong forcing can produce convective clouds that use the higher CAPE and shear available to produce organized convection. Gonçalves et al. (2015) show that increased RRs (radar reflectivity values larger than 35 dBZ) during the dry season mainly occur over higher elevations in Amazonas (section 3.2.1). The higher CINE and smaller amount of water vapour reduces the occurrence of convection, but when convection is able to develop, it has all the ingredients to be deeper. Machado et al. (2004) explain that the more intense convective clouds during the dry to wet season transition may result from less competition of surface moisture convergence to feed cumulonimbus clouds because a smaller number of rain cells exist. Figure 2f presents the RR statistics for 2014 and the monthly rainfall measured by rain gauge in T3.

### 3.1.2 Size Distribution of Cloud Clusters and Rain Cells

Cloud clusters and rain cell data were derived from GOES-13 satellite images and S-band radar using the ForTraCC (Forecasting and Tracking Cloud Clusters see Vila et al., 2008) algorithm. A cloud cluster is defined by connected ensembles of pixels with brightness temperatures (BT) for the 10.5 μm channel that are colder than 235 K, as defined by Machado et al. (1988). A rain cell is defined as a connected ensemble of pixels in the radar 2.5 km CAPPI with reflectivity larger than 20 dBZ. Quite often, rain cells, which are embedded in cloud clusters, are observed when clouds start to form raindrops. The average cloud cluster size and lifespan are 75-km effective radius (hereafter called radius) and 1.5 hours, respectively, during the wet and dry seasons in the Amazon. The typical rain cell has a 7.5-km radius and a 0.6-hour lifespan. On average, cloud clusters are 10 times larger and have lifespans of approximately three times that of their associated rain cells. These are average characteristics; cloud clusters come in a wide range of sizes. Cloud clusters can exceed 300 km in radius and have a lifespan longer than 24 h, while rain cells can grow to up to approximately 60 km in radius and last for a couple of hours. Figure 3

shows the dry and wet season cloud clusters and rain cell size distributions identified in this study, as well as the differences between them. The basic size distribution does not vary substantially between the two seasons because cloud cluster size distribution follows an exponential distribution, as shown by Machado et al. (1992); however, certain distinctions can be noted if the difference is computed. The wet season has more small and large rain cells and cloud clusters than the dry season. The dry season produces more rain cells in the range of a 10-km radius and cloud clusters of an approximately 40-km radius. The ratio between the cloud cluster and rain cell average radii during the wet season is much greater because of the larger stratiform cloud decks typical of a monsoon cloud regime. The thermodynamics of the dry season environment discussed in the preceding section favour the organization of more compact and active convection with more intense rainfall events but accumulated rainfall amounts that are 4 times smaller.

### 3.1.3 Mass-Weighted Mean Rainfall Diameter for the Dry and Wet Seasons

Variations in cloud processes between the two Amazonian seasons were evaluated in this study in order to determine whether important microphysical differences between raindrops during the wet and dry seasons exist, or whether only RR and rainfall frequency vary between seasons. These features were investigated through the deployment of disdrometers and a dual-polarimetric radar. This study focuses on rainfall and raindrops; however, seasonal differences in cloud droplet size distributions may warrant attention as well.

For instance, the effect of aerosol concentrations on cloud droplets in shallow convective clouds, where aerosols generally reduce the size and increase the concentration of a given liquid water content, is well known (Cecchini et al., 2016, among several other studies). However, if a polluted cloud transitions from shallow-to-deep convection, aerosols can invigorate clouds (Rosenfeld et al., 2008; Koren et al., 2012; Gonçalves et al., 2015). Giangrande et al. (2017) present the G1 airplane cloud particle distribution measurements taken during GoAmazon2014/5 and show the predominance of larger cloud droplets in warm clouds during the wet season. The in situ cloud droplet data were collected for a shallow cloud population. The result is very different when seasonal data collected using disdrometers that measure raindrops at least 100 times larger (measured as mass-weighted mean diameter ($D_m$)) are compared. Given that raindrop diameter depends on RR, which varies between the two seasons, dry and wet season $D_m$ values were compared as a function of RR in 5 mm $h^{-1}$ intervals. Different frequencies of convective and stratiform clouds during the wet and dry seasons also merit evaluation. As discussed by Giangrande et al. (2017), stratiform clouds occur more often in the wet season than the dry season; hence, $D_m$ should be evaluated separately for convective and stratiform clouds. The cloud classification employed in this study was performed using the radar wind profiler (RWP) and ancillary data as described by Giangrande et al. (2017) from March 2014 to December 2015. Clouds were classified based on the predominant cloud type in the warm cloud layer. Convective clouds include strong and weak convection, while stratiform clouds include those with and without a well-defined bright band.

Figures 4a and 4b show the $D_m$ for the wet and dry seasons as functions of the RR for convective and stratiform clouds. The arrows on the x-axis mark distributions where the averages vary given a statistical significance of 95%. For convective clouds,

the mass-weighted mean diameter is larger during the dry season for a given RR. This result suggests the different cloud processes generate larger rainfall drops. The differences in shallow clouds during the dry season may be due to the reduced humidity, as shown in Figure 2c, which can reduce supersaturation and increase droplet evaporation via entrainment. However, if a cloud evolves into the deep convective stage, the higher cloud base, shear, and CAPE induce stronger vertical motion and mesoscale organization, generating higher quantities of ice (shown in next section) and forming larger raindrops through melting of large ice particles such as snow and graupel. For stratiform clouds (Figure 4b), the difference between the two seasons is much smaller and significant only for very low RRs.

#### 3.1.4 Cloud Vertical Profiles for the Dry and Wet Seasons

The results presented above discuss rainfall at the surface level. To better understand the cloud processes associated with the dry and wet seasons we must evaluate the hydrometeor vertical profiles of precipitating clouds. An X-band dual-polarization radar was installed at the T3 site and operated during the GoAmazon2014/5 IOPS in February-March and September-October 2014. To account for potential wet radome attenuation effects and obtain useful dual-polarization measurements with sufficient vertical coverage, the data analysed included only cases without rain over the radar and collected within the 10- and 60-km radius range. As described in the methodology section, the volume scan was processed with attenuation correction and a ZDR offset to build contoured frequency by altitude diagrams (CFAD) of reflectivity (Z), specific differential phase (KDP), differential reflectivity (ZDR), and the horizontal and vertical correlation coefficient for the consistency of the H and V returned power and phase of each pulse for both the wet and dry seasons.

Figure 5 shows the reflectivity CFAD for the wet and dry seasons. The typical stratiform and convective patterns for the wet and dry seasons are clearly visible. For the wet season, the bright band is very clear and has a pronounced peak at approximately 4 km, which corresponds to the layer where ice melts and reflectivity increases. Moreover, the levels above the melting layer have less intense reflectivity, demonstrating the less intense convective process that occurs in the majority of cases during the wet season. For the dry season, the typical convective profile with a higher reflectivity in the lower levels corroborates the higher RRs observed during this season. In addition, the mixed and glaciated layers exhibit more frequent high reflectivity values, indicating the presence of large ice hydrometeors.

Figure 6 shows the CFAD for the dual-polarization parameters, ZDR, KDP and co-polar correlation coefficient. The hydrometeor response to the transmitted signal depends on several factors that may alter certain characteristics of the measured signal, such as hydrometeor orientation by the electrification field (see Mattos et al., 2017 for a detailed discussion), ice density, and crystal shape. Of course, there are also other possible effects that may impact the data quality, such as resonance and partial beam-filling. Although the CFADs are not completely different, given that these parameters have a small range of variation and are subject to the limitations described above, some clear seasonal differences can be observed. The ZDR that largely reflects ice orientation contains a greater number of near-zero or negative signals during the dry season compared to the wet season. This is likely associated with crystal orientation by the electrical field, as more lightning occurs (see Williams

et al., 2002) and more vertically oriented ice shapes such as graupel may occur during the dry season than the wet season. The KDP distribution shows considerably larger values in the warm layer during the dry compared to the wet season, indicating that the higher RRs and greater number of positive values in the mixed phase are probably associated with intense updrafts, as shown by Giangrande et al. (2016). The correlation coefficient highlights an interesting feature. During the dry season, there appears to be a clearer distinction between the mixed phase and the glaciation phase above 8 km. The wet season correlation coefficient is more homogenous with height inside the cloud. Cecchini et al. (2017b) and Jakel et al. (2017) discuss the greater efficiency of clouds forming in a clean environment to produce ice. The dry season exhibits higher average correlations at approximately 8 km, demonstrating a deeper and unmixed water layer at these heights. This likely indicates that clouds forming during the wet season have a smaller mixed phase than clouds forming during the dry season and under poor air quality conditions.

### 3.2 Rainfall Sensitives to Aerosols, Topography, and Vegetation

This section presents rainfall sensitivities to different surface types, topography and aerosol concentrations. Ancillary data describing vegetation type, topography and aerosol concentrations, as well as measurements from the HALO airplane, are employed to study the total rainfall, RR, cloud droplet and raindrop sensitivities to these environmental and geographic characteristics.

#### 3.2.1 Rainfall $D_m$ as a Function of Rainfall Rate for Polluted and Clean Cases

The impact of aerosol concentration on cloud microphysical properties needs to be analysed for the different seasons. Particle concentrations measured at the surface using the CPC during the dry and wet seasons vary greatly from one another. For instance, the 33$^{rd}$ and 66$^{th}$ percentiles are 673 cm-3 and 1377 cm-3 for the wet season and 1954 cm$^{-3}$ and 3392 cm$^{-3}$ for the dry season, respectively. Nearly three times as many aerosols are present during the dry compared to the wet season, which can have substantial implications for cloud and rainfall formation. However, as shown in Figure 2, the thermodynamic characteristics also vary greatly, and the differences cannot be explained only by the difference in aerosol concentrations. To evaluate the impact of aerosols on cloud processes, the mass-weighted mean rainfall diameter must be evaluated for different particle concentrations during each season. However, after analysis, this comparison was only possible during the wet season because rainfall events with particle concentrations exceeding 66$^{th}$ percentile in the dry season were rare. During the dry season, the upper one-third of aerosol concentrations are characterized mostly by drier days. The dry season is characterized by biomass burning and approximately 6 times more mass-loaded (organic) aerosols than during the wet season. Shilling et al. (2018) describe the typical aerosol types and the evolution of organic aerosol particles during the wet and dry season in the Manaus pollution plume. Figure 7 shows the $D_m$ during the wet season for background (particle concentrations less than the 33$^{rd}$ percentile) and polluted (particle concentrations greater than the 66$^{th}$ percentile) conditions as a function of RR. This

calculation requires two different instruments to be co-located. Therefore, the number of samples from each 5-minute continuous rainfall event interval, in each RR class was drastically reduced. Consequently, the differences between the two air quality categories in each RR bin were significant only at the 85% level. Even if the differences between the two average values for background and polluted cases are not significant, the physical results show clear trends. For low RRs, which are more often associated with warm cloud processes, the cases with background aerosol concentrations have a larger $D_m$ because there are fewer CCN and lower cloud droplet concentrations, resulting in large raindrops. However, for greater RRs, which are typically associated with deep convection, the $D_m$ is greater for polluted clouds, demonstrating the major effect of convective invigoration discussed in the preceding section. Rosenfeld and Ulbrich (2003) used satellite data to estimate raindrop size distributions for continental and maritime Amazon clouds (LBA). They found that clouds over the continent produce greater concentrations of large drops and smaller concentrations of small drops. They suggested that this behaviour is caused by the effects of aerosols on precipitation formation processes.

### 3.2.2 Rainfall Sensitivity to Surface Cover

There is a very complex diurnal cycle over the Amazonas basin. Burleyson et al. (2016) used 15 years of satellite data to show a heterogeneous spatial distribution of convection that results from numerous local effects of rivers and vegetation cover. Using radar data, Saraiva et al. (2016) also found the Amazonas diurnal cycle to vary regionally. In addition to the natural geographic effect, rainfall modulation occurs through anthropogenic-induced changes in vegetation and the presence of large cities. Durieux et al. (2003) have shown that cloud cover varies as a function of the deforestation pattern. Lin et al. (2010), among several other studies, have discussed the urban heat island effect on the region's climate. To understand how vegetation cover influences precipitation characteristics, two approaches were applied: one using statistical radar data and the other using a special HALO mission specifically aimed at this topic.

For the statistical approach, the RR was calculated from the SIPAM S-band radar data for the dry and wet seasons, as described in Section 2. Surface cover was obtained from the digital Terra-Class classification data (Almeida et al., 2016). This database contains 15 vegetation classes, such as forest; hydrology; urban areas; and several deforestation classes, including clean and dirty pasture, deforested areas, and exposed soil, among others. These classes were regrouped in four categories for this study: forest (covering 76.9% of the studied region), hydrography (16.3%), non-forest (6.2%), and urban area (0.5%). These two datasets were combined to evaluate the different RRs for each surface cover type. Terra-Class has 300 m resolution and was interpolated to the radar grid using the most frequent surface type class. Figure 8 presents the spatial distribution of the vegetation classes (Figure 8a) over the 150 km radius of the S-band radar and the topography of the region (Figure 8b).

Figure 9 shows the RR box plots for each surface type in the wet and dry seasons. This analysis does not consider cloud life cycle or the different thermodynamic or dynamic conditions that may have been present and only considers those statistics present among the different surface types. The different behaviours are a consequence of different physical processes, which will be discussed in this section.

For the wet season, the RR varies little among the different surface cover classes. However, for the dry season, a greater amount of rainfall occurred over the urban areas and smaller amounts occurred over non-forested regions. In general, the dry season RR was greater than that in the wet season. The median and tail of the distribution were larger over urban areas and smaller over deforested areas. The difference between the median values of non-forested and urban RRs in the dry season was approximately 25%. Although the number of radar pixels in each class varied and the urban area represents only 0.5% of the area, the box plot patterns are different. The smaller differences during the wet season can be expected because rainfall during this season has a strong stratiform cloud component typical of a monsoon rainfall regime, as described above. In this type of regime, large-scale dynamic forcing is very strong, and surface type has little impact. However, during the dry season, rainfall events largely depend on local forcing and surface latent heat flux. Manaus, as an urban centre, is characterized by a strong heat island effect (Souza and Alvala, 2014) that creates a convergence fed by moisture from the surrounding forest. The non-forested area has less available latent heating than the forest, which may contribute to lower RRs. These results are associated with RR and not total rainfall data. Total rainfall is larger over the forest and hydrology areas (not shown).

Fisch et al. (2004) have discussed the differences in the boundary layer between forest and pasture. They show, for the Amazonas dry season, that the height of the fully developed convective boundary layer over forest is approximately 1100 m, and it is approximately 50% higher over pasture. During the wet season, the forest and pasture have nearly the same boundary layer height (approximately 1000 m). Does the different thermodynamic behaviour during the dry season result in different cloud microphysical properties and, consequently, different radiative forcing? This is a very important question because climate change simulations in Amazonas need to correctly reproduce the cloud processes over each of these surface covers. The results presented above consider RR and the impacts of the surface on clouds. Several physical processes play an important role in the generation of the different RRs between different surface types, such as the boundary layers described above. The effect of surface type on cloud droplet distribution under shallow convection conditions is not well understood. One of the ACRIDICON-CHUVA HALO missions was especially designed to investigate this relationship. Cloud processes for different surface covers may be evaluated from a statistical point of view as a function of the surface cover using a combination of data from several different flights. However, airplane flights are limited to a few hours and measure clouds for different meteorological conditions, heights, thermodynamic conditions, and aerosol loadings that, as already stated in the set of papers published using the GoAmazon data, have a strong impact on cloud microphysical properties. Therefore, a specific flight mission was designed to evaluate this matter. The AC17 flight, which was completed on 27 September 2014, looked at the contrast between clouds above forest and pasture surfaces. The objectives were to observe and compare macrophysical and microphysical cloud properties over both forest and pasture areas under comparable environmental conditions. As the flight legs occurred at the same fixed level, the thermodynamics and aerosol concentrations were nearly the same due to the short flight time and path (40 km) in each region. The two flight leg paths are shown in Figure 10. Cloud profiling was carried out over both 40-km legs (red lines in Figure 10), which included forested, transition, and pasture surface covers. The flight plan for the cloud profiling legs was designed for a fixed altitude level for each leg in order to profile clouds along the trajectories. The flight level was selected as a function of the cloud development at the local time for each flight leg. Leg 1 occurred at

1500 UTC (11:00 LST) and leg 2 at 1700 UTC (13:00 LST). The height of the flights employed in this study were 1500 m, 1900 m and 2500 m. In leg 2, the cloud base was higher and the clouds were measured at 1900 m and 2500 m. In Figure 10, the GOES visible image shows the increase in cloud cover from the first flight to the second, as well as the typical shallow cumulus clouds measured. During the morning leg 1 flight, the cloud base was nearly the same over both the forested and non-forested areas; however, during the afternoon flight, the cloud base over the non-forested area appeared to be slightly higher than that over the forested area. Therefore, some differences among clouds can also be related to measurements taken at the same height but in a different cloud layer.

Only 350 seconds of measurements from each region and at each flight level were used in this analysis. Data from the beginning of the flight over the forest, the boundary between the forested and deforested region, and the final flight path over the deforested region were discarded so that only data from the centres of the forested and deforested regions were evaluated. Figure 11a shows a scatter plot of the cloud droplet concentration and liquid water content for flight leg 1 over the forest and pasture at approximately 1500 m, 1900 m and 2500 m. These data show a nearly linear relationship, with a correlation coefficient ranging from 0.94 to 0.99 for the relationship between cloud droplet concentration and liquid water content at varying heights. For a fixed cloud droplet concentration, clouds over the forested area have more liquid water than clouds over pasture at the same height. This means cloud droplets that develop over rain forests are larger than those that evolve over pastures. Therefore, cloud droplet size distribution is different between the two regions, with forested areas producing larger cloud droplets.

Figure 12 shows the cumulative histogram of the CCN concentrations ($N_{CCN}$) for the two legs over the forested and non-forested regions at approximately 1500, 1900 and 2500 m. The decrease in $N_{CCN}$ with altitude for boundary layer aerosols agrees with the other flights carried out during the ACRIDICON-CHUVA campaign, as shown in Andreae et al. (2017). The magnitude of the $N_{CCN}$ is typical for polluted regions in Brazil and falls between strong biomass burning events and forested regions far away from biomass burning events. For leg 1, $N_{CCN}$ distribution is nearly identical at the 1500 and 1900 m flight heights for both the forested and non-forest regions; however at 2500 m, the distributions are quite different, with the non-forested region exhibiting a greater $N_{CCN}$. For leg 2, the difference between the two surface types is larger, and the non-forested regions exhibited higher $N_{CCN}$ than the forested region at all altitudes. In the first leg, the difference between forested and deforested regions increased with altitude, and the deforested regions exhibited greater $N_{CCN}$. Two factors should be considered: leg 1 occurred approximately 11:00 LST; therefore, the convective boundary layer was not fully developed, and at 2500 m, the measurements likely represent the residual boundary layer from the previous day. Leg 2 occurred later, at approximately 13:00 LST, when the boundary layer was deeper and well mixed. Another important factor is the regional wind direction from east; for leg 1, the air over the forest was the air advected from the deforested region, and for leg 2, a north-south transect flight, the air was advected from the homogenous forest along the easterly side.

The cloud microphysics differences between the forested and deforested clouds are probably related to these differences in the $N_{CCN}$ distributions. Some clouds over pastures have the same liquid water quantities as clouds over forests, although the pasture clouds contained higher cloud droplet concentrations. This could result from several processes, such as larger vertical motion

induced by the higher sensible heating, by the large aerosol concentration over pasture and/or the high-water availability over the forest.

Figures 11b and 11c show the $D_m$ and cloud droplet concentrations as a function of vertical motion. These figures illustrate that the larger cloud droplet diameter samples over the forest and the larger cloud droplet concentrations increase with vertical velocity (updraft and downdraft), but there is not a clear relationship between vertical velocity and $D_m$. Vertical velocity increases supersaturation but does not appear to modulate droplet size. Cecchini et al. (2017a) also found that different flights demonstrated a small correlation between vertical motion and droplet size. Nevertheless, cloud droplet concentrations are more linearly related to vertical motion (correlation coefficient is approximately 0.6). The stronger the updrafts are, the higher the droplet concentration is. This relationship does not appear to show differences between forested and pasture areas.

### 3.2.3 Rainfall Sensitivity to Topography

The topography database employed in this study included the digital elevation data from NASA Shuttle Radar Topographic Mission and has a resolution of 90 m at the equator (Jarvis et al., 2008). Figure 8 shows the topographic spatial distribution within the 150 km radius of the radar's coverage. As the sample size decreased logarithmically relative to elevation increases, the classes were binned in log intervals as follows: from 0 to 15 m, from 15 to 40 m, from 40 to 83 m and from 83 to 157 m. Using the S-band radar data, a statistical box plot was constructed for each topography class (Figure 13). For the wet season, the statistics are nearly the same for all topography classes. The highest topography class shows nearly the same median but a slightly smaller tail distribution. However, for the dry season, considerable differences are found among the topography classes. The higher the land surface, the longer the RR distribution tail. During the dry season, convective inhibition is higher, as shown in Figure 2, and cloud formation requires some kind of forcing to overcome this inhibition and take advantage of the higher CAPE available during this season. Topography is one forcing mechanism that allows this to occur, even if the differences are only a few hundred metres.

## 4. Summary and Conclusions

The Amazonas climate is comprised of distinctive and complex interactions between a multitude of different physical processes that result in one of the most important rainfall production systems on Earth. Interannual variability is high, and in recent years, the driest and wettest years on record have been observed. El Niño, La Niña, and Atlantic Ocean temperatures are some of the interannual features affecting total rainfall. In addition, many synoptic conditions affect large-scale rainfall mechanisms. These are the ingredients necessary to generate large amounts of rainfall in Amazonas, and they are normally organized in mesoscale convective systems. Cloud and precipitation systems differ during the wet and dry seasons. Total rainfall in the wet season is 4.2 times larger than that in the dry season, but RRs observed during the dry season are approximately 22% higher than those that occur in the wet season. The wet season has a smaller CAPE, CINE, vertical wind shear, and cloud base height and a

greater amount of integrated water vapour than the dry season. The wet season typically has monsoon-type rainfall, while convection occurs at a smaller scale during the dry season. The typical cloud cluster in Amazonas (wet and dry season) has an effective radius of approximately 75 km and a 1.5-hour life cycle. The rain cells inside these cloud clusters have an average radius of approximately 7.5 km and a 0.6-hour life cycle. Seasonality also modulates the size distribution of these features. The wet season has more small and large cloud clusters and rain cells, which are typical of isolated cumuliform convection and monsoon rainfall cloud organization. The dry season has proportionally more cloud clusters and rain cells of approximately 40 km and 10 km radii, respectively, favouring a cloud organization that is reduced in size but larger than that of isolated convection. The differences between the two seasons are also observed in the microphysics of the clouds. Rainfall drops are larger in convective clouds during the dry season than during the wet season, likely due to enhanced ice processes. For stratiform clouds, larger drops are also observed but are not statistically significantly different.

The cloud hydrometeor vertical profile signature was evaluated for the first time in Amazonas in this study. X-band dual-polarization radar data were used to provide dual-polarization CFAD variables for the dry and wet seasons. As expected, there are differences between the dual-polarization statistical distributions between the seasons. The wet season cloud type has a typical bright band at approximately 4 km altitude. The dry season has a stronger reflectivity below and above the melting layer, which is characteristic of the liquid water and ice profiles of stronger convective clouds. The ZDR profile of the dry season indicates more vertically oriented ice, while the KDP profile revealed larger positive values in the mixed phase, consistent with more frequent and stronger updrafts. During the dry season, the correlation coefficient indicated more heterogeneous clouds above the melting layer, with two distinct layers above and below 8-km height. This indicates a clear characterization of the mixed phase and glaciation layers.

The evaluation of the effect of aerosol concentrations on raindrop size distribution shows an interesting feature. Due to the small statistical sample of rainfall events during the dry season for different ranges of aerosol loading, it was only possible to evaluate the aerosol effect during the wet season. Clean cases show larger raindrops for lower RRs, and polluted cases show larger raindrops for a higher RRs. For a RR less than 8 mm $h^{-1}$, the typical warm rain and less organized convective rainfall events, the clean cases have a more straightforward interpretation based on the small number of CCN and consequently larger droplets. However, when convection becomes deeper with increased RRs, the polluted cases seem to invigorate convection, as suggested by Rosenfeld et al. (2008).

General statistics for how surface type impacts RR were significant only for the dry season. The wet season did not exhibit different RRs for different surface types. For the dry season, urban regions had the highest RR, and deforested regions had the lowest. This is probably related to the Manaus heat island effect, with moisture provided by the surrounding forested area and smaller latent heating fluxes in large deforested areas, respectively. Nearly identical cloud properties were measured by the HALO airplane over the forested and deforested areas. The specific flight design, which allowed for an evaluation of the microphysical differences in shallow convective cloud formation, provided unprecedented data to study these differences under nearly the same synoptic and environmental conditions. Nearly simultaneous flight legs at the same height, along a short path of only 40 km, allowed us to compare cloud processes over different surfaces types. As a result, clouds over forested areas

were observed to have larger cloud droplets, and in general, the vertical velocity was well correlated with cloud droplet concentrations. However, these data did not correlate with mass-weighted mean cloud droplet diameter.

Finally, the impact of topography on the RR was evaluated. There was no difference in the RR during the wet season for different topography classes. For the dry season, there was a clear increase in the RR as elevation increased. This was probably related to the topographical forcing required to overcome the large CINE and take advantage of the large CAPE available during this season.

The GoAmazon dataset brings new insights into the process of cloud and rainfall formation in the Amazon and to those complexities requiring further research. is the entire dataset is likely to have a very high potential impact on the modelling of aerosol, cloud, and landscape features in tropical scenarios. Nevertheless, there are several areas that still necessitate further research to complete the picture of cloud processes in Amazonas. For instance, a detailed microphysical description of clouds as a function of the two patterns of convection, cumuliform and deep convection, is still wanting (see Wang et al., 2018). Changes in the microphysical properties and mixed phase are some of the unknown behaviours of cloud processes. How these processes change as function of the season, cloud life cycle, aerosol loading, and topography are some examples of areas in need of further research to improve the cloud modelling over continental tropical regions. Another potential area for future study includes the implications and solutions for GCMs, which may not resolve subtle variations in topography but are very important in triggering convection during the dry season.

*Acknowledgements:* We thank all participants in the GoAmazon2014/5 and ACRIDICON-CHUVA for their cooperation and for making this study possible. We acknowledge FAPESP (São Paulo Research Foundation) Projects 2009/15235-8, 2014/08615-7 and 2015/14497-0. This work was conducted under scientific licenses 001030/2012-4, 001262/2012-2 and 00254/2013-9 of the Brazilian National Council for Scientific and Technological Development (CNPq). Institutional support was provided by the Central Office of the Large-Scale Biosphere Atmosphere Experiment in Amazonia (LBA), the National Institute of Amazonian Research (INPA), the National Institute for Space Research (INPE), Amazonas State University (UEA), and the Brazil Space Agency (AEB). We acknowledge the support of the Max Planck Society, the German Aerospace Centre (DLR), and the German Science Foundation (Deutsche Forschungsgemeinschaft, DFG) within the DFG Priority Program SPP 1294 for the ACRIDICON-CHUVA campaign. We also acknowledge the Atmospheric Radiation Measurement (ARM) Climate Research Facility, a user facility of the U.S. DOE, Office of Science, sponsored by the Office of Biological and Environmental Research, and support from the ASR program. J. Fan was supported by the Climate Model Development and Validation program funded by the Office of Biological and Environmental Research in the US Department of Energy Office of Science. R. Albrecht was supported by CNPq 459546/2014-7. We acknowledge Dr. Y. Zhuang and anonymous reviewers for their comments and suggestions.

## References


Adams, Adams, D. K., Barbosa, H. M. J., and De Los Rios, K. P. C.: A spatiotemporal water vapor/deep convection correlation metric derived from the Amazon Dense GNSS Meteorological Network, Monthly Weather Review, http://dx.doi.org/10.1175/MWR-D-16-0140.1, 2016.

Albrecht, R. I., Morales, C. A., and Silva Dias, M. A. F.: Electrification of precipitating systems over the Amazon: Physical processes of thunderstorm development, Journal of Geophysical Research, 116, D08209, doi:10.1029/2010JD014756, 2011.

Almeida, C.A., Coutinho, A.C., Esquerdo, J.C.D.M., Adami, M., Venturieri, A., Diniz, C.G., Dessay, N., Durieux, L., and Gomes, A.R.: High spatial resolution land use and land cover mapping of the Brazilian Legal Amazon in 2008 using Landsat-5/TM and MODIS data, In: Acta Amazonica, 46(3), 291-302, http://www.inpe.br/cra/projetos_pesquisas/dados_terraclass.php, 2016.

Andreae, M. O., Afchine, A., Albrecht, R., Holanda, B. A., Artaxo, P., Barbosa, H. M. J., Bormann, S., Cecchini, M. A., Costa, A., Dollner, M., Fütterer, D., Järvinen, E., Jurkat, T., Klimach, T., Konemann, T., Knote, C., Krämer, M., Krisna, T., Machado, L. A. T., Mertes, S., Minikin, A., Pöhlker, C., Pöhlker, M. L., Pöschl, U., Rosenfeld, D., Sauer, D., Schlager, H., Schnaiter, M., Schneider, J., Schulz, C., Spanu, A., Sperling, V. B., Voigt, C., Walser, A., Wang, J., Weinzierl, B., Wendisch, M., and Ziereis, H.: Aerosol characteristics and particle production in the upper troposphere over the Amazon Basin, Atmos. Chem. Phys. Discuss., https://doi.org/10.5194/acp-2017-694, in review, 2017.

Andreae, M. O., Artaxo, P., Fischer, H., Freitas, S. R., Lelieveld, J., Dias, M. A. F. S., Freitas, S., and Longo, K. M., Strom, J.: Transport of biomass burning smoke to the upper troposphere by deep convection in the equatorial region, Journal of Geophysical Research, 28(6), 951-954, 2001.

Andreae, M.O., Rosenfeld, D., Artaxo, P., Costa, A. A., Frank, G. P., Longo, K. M., and Silva Dias, M. A.: Smoking rain clouds over the Amazon. Science, 303, 1337-1342, 2004.

Artaxo, P, Martins, J. V. , Yamasoe, M. A. , Procópio, A. S. , Pauliquevis, T. M. , Andreae, M. O. , Guyon, P. , Gatti, L. V., and Leal, A. M. C.: Physical and chemical properties of aerosols in the wet and dry season in Rondonia, Amazonia, Journal of Geophysical Research, 107, 8081-8095, 2002.

Betts, A. K., L. V. Gatti, Cordova, A. M., and Silva Dias, M. A. F., Fuentes, J. D.: Transport of ozone to the surface by convective downdrafts at night, Journal of Geophysical Research, 107, 1–13, 2002.

Braga, R. C., Rosenfeld, D., Weigel, R., Jurkat, T., Andreae, M. O., Wendisch, M., Pöhlker, M. L., Klimach, T., Pöschl, U., Pöhlker, C., Voigt, C., Mahnke, C., Borrmann, S., Albrecht, R. I., Molleker, S., Vila, D. A., Machado, L. A. T., and Artaxo, P.: Comparing parameterized versus measured microphysical properties of tropical convective cloud bases during the ACRIDICON–CHUVA campaign, Atmos. Chem. Phys., 17, 7365-7386, https://doi.org/10.5194/acp-17-7365-2017, 2017.

Bringi, V. N., Huang, G.-J., Chandrasekar, V., and Gorgucci, E.: A methodology for estimating the parameters of a gamma raindrop size distribution model from polarimetric radar data: Application to a squall-line event from the TRMM/Brazil campaign, J. Atmos. Oceanic Technol., 19, 633–645, 2002.

Burleyson, C., Feng, Z., Hagos, S., Fast, J., Machado, L., and Martin, S.: Spatial Variability of the Background Diurnal Cycle of Deep Convection around the GoAmazon2014/5 Field Campaign Sites, J. Appl. Meteorol. Clim., 55, 1579–1598, doi:10.1175/JAMC-D-15-0229.1, 2016.

Camponogara, G., Silva Dias, M. A. F., and Carrió, G. G.: Relationship between Amazon biomass burning aerosols and rainfall over the La Plata Basin, Atmos. Chem. Phys., 14, 4397-4407, 2014.

Cavalcanti, I. F. A., Ferreira, N. J., and Silva, M. G. A. J. (Eds.): Weather and Climate in Brazil (Tempo e Clima no Brasil - in Portuguese), Oficina Texto, 463, 2009.

Cecchini, M. A., Machado, L. A. T., Andreae, M. O., Martin, S. T., Albrecht, R. I., Artaxo, P., Barbosa, H. M. J., Borrmann, S., Fütterer, D., Jurkat, T., Mahnke, C., Minikin, A., Molleker, S., Pöhlker, M. L., Pöschl, U., Rosenfeld, D., Voigt, C., Weinzierl, B., and Wendisch, M.: Sensitivities of Amazonian clouds to aerosols and updraft speed, Atmos. Chem. Phys., 17, 10037-10050, https://doi.org/10.5194/acp-17-10037-2017, 2017a.

Cecchini, M. A., Machado, L. A. T., Comstock, J. M., Mei, F., Wang, J., Fan, J., Tomlinson, J. M., Schmid, B., Albrecht, R., Martin, S. T., and Artaxo, P.: Impacts of the Manaus pollution plume on the microphysical properties of Amazonian warm-phase clouds in the wet season, Atmos. Chem. Phys., 16, 7029-7041, https://doi.org/10.5194/acp-16-7029-2016, 2016.

Cecchini, M. A., Machado, L. A. T., Wendisch, M., Costa, A., Krämer, M., Andreae, M. O., Afchine, A., Albrecht, R. I., Artaxo, P., Borrmann, S., Fütterer, D., Klimach, T., Mahnke, C., Martin, S. T., Minikin, A., Molleker, S., Pardo, L. H., Pöhlker, C., Pöhlker, M. L., Pöschl, U., Rosenfeld, D., and Weinzierl, B.: Illustration of microphysical processes in Amazonian deep convective clouds in the Gamma phase space: Introduction and potential applications, Atmos. Chem. Phys. Discuss., https://doi.org/10.5194/acp-2017-185, in review, 2017b.

Cifelli, R., Petersen, W. A., Carey, L. D., Rutledge, S. A., and Silva Dias, M. A. F.: Radar observations of kinematic, microphysical, and precipitation characteristics of two MCSs in TRMM-LBA, Journal of Geophysical Research, 107, doi:10.1029/2000JD000264, 2002.

Cohen, J. C. P., Silva Dias, M. A. F., and Nobre, C. A.: Environmental conditions associated with Amazonian squall lines: A case study. Monthly Weather Review, 123, 3163-3174, 1995.

Diedhiou, A., Machado, L. A. T., and Laurent, H.: Mean kinematic characteristics of synoptic easterly disturbances over the Atlantic, Advances in Atmospheric Sciences, 27, 483–499, 2010.

Dos Santos, M.J.; Silva Dias, M.A.F.; and Freitas, E.D.: Influence of local circulations on wind, moisture, and precipitation close to Manaus City, Amazon Region, Brazil, J. Geophys. Res. Atmospheres, 119, 233–249, doi:10.1002/2014JD021969, 2014.

Durieux, L., Machado, L.A.T., and Laurent, H.: The impact of deforestation on cloud cover over the Amazon arc of deforestation, Remote Sens. Environ., 86, 132-140, 2003.

Fisch, G., Tota, J., Machado, L. A. T., Silva Dias, M. A. F., Lyra, R. F., Nobre, C. A., Dolman, A. J., and Gash, J. H. C.: The convective boundary layer over pasture and forest in Amazonia, Theor. Appl. Climatol. 78, 47–59, doi:10.1007/s00704-004-0043-x, 2004.

Fitzjarrald, D. R., Sakai, R. K., Moraes, O. L. L., Oliveira, R. C., Acevedo, O. C., Czikowsky, M. J., and Beldini, T.: Spatial and temporal rainfall variability near the Amazon–Tapajós confluence, J. Geophys. Res., 113, G00B11, doi:10.1029/2007JG000596, 2008.

Freitas, S. R., Longo, K. M., Silva Dias, M., Silva Dias, P., Chatfield, R., Prins, E., Artaxo, P., Grell, G., and Recuero, F.: Monitoring the transport of biomass burning emissions in South America, Environmental Fluid Mechanics, 5, 135–167, doi:10.1007/s10652-005-0243-7, 2005.

Freitas, S.R., Panetta, J., Longo, K. M., Rodrigues, L. F., Moreira, D. S., Rosário, N. E., Silva Dias, P. L., Silva Dias, M. A. F., Souza, E. P., Freitas, E. D., Longo, M., Frassoni, A., Fazenda, A. L., Santos e Silva, C. M., Pavani, C. A. B., Eiras, D., França, D. A., Massaru, D., Silva, F. B., Cavalcante, F., Pereira, G., Camponogara, G., Ferrada, Gonzalo A., Campos Velho, H. F., Menezes, I., Freire, J. L., Alonso, M. F., Gácita, M. S., Zarzur, M., Fonseca, R. M., Lima, R. S., Siqueira, R. A., Braz, R., Tomita, S., Oliveira, V., Martins, L. D.: The Brazilian developments on the Regional Atmospheric Modeling System (BRAMS 5.2): an integrated environmental model tuned for tropical areas, Geoscientific Model Development Discussions, 130, 1-55, 2016.

Fu, R., Yin, L., Li, W., Arias, P.A., Dickinson, R.E., Huang, L., Chakraborty, S., Fernandes, K., Liebmann, B., Fisher, R., Myneni, R.B,. Increased dry-season length over southern Amazonia in recent decades and its implication for future climate projection. Proceedings of the National Academy of Sciences 110, 18110–18115. doi: 10.1073/pnas.1302584110, 2013.

Garstang, M., Massie, H. L., Halverson, Jr. J., Greco, S., and Scala, J.: Amazon coastal squall lines. Part 1: Structure and kinematics, Monthly Weather Review, 122, 608-622, 1994.

Gash, J. H. C., Nobre, A., Roberts, J. M., and Victoria, R. L. (Eds.): An overview of ABRACOS, in Amazon Deforestation and Climate, John Wiley, New York, 1996.

Gerken, T., Wei, D., Chase, R. J., Fuentes, J. D., Schumacher, C., Machado, L. A. T., Andreoli, R. V., Chamecki, M., Souza, R. A. F., Freire, L. S., Jardine, A. B., Manzi, A. O., Santos, R. M. N., Randow, C. V., Costa, P. S., Stoy, P. C., Tóta, J., and Trowbridge, A. M.: Downward transport of ozone rich air and implications for atmospheric chemistry in the Amazon rainforest, Atmos. Environ. Part A, 124, 64–76, doi:10.1016/j.atmosenv.2015.11.014, 2015.

Giangrande, S. E., Feng, Z., Jensen, M. P., Comstock, J., Johnson, K. L., Toto, T., Wang, M., Burleyson, C., Mei, F., Machado, L. A. T., Manzi, A., Xie, S., Tang, S., Silva Dias, M. A. F., de Souza, R. A. F., Schumacher, C., and Martin, S. T.: Cloud Characteristics, Thermodynamic Controls and Radiative Impacts During the Observations and Modeling of the Green Ocean Amazon (GoAmazon2014/5) Experiment, Atmos. Chem. Phys. Discuss., https://doi.org/10.5194/acp-2017-452, in review, 2017.

Giangrande, S. E., Toto, T., Jensen, M. P., Bartholomew, M. J., Feng, Z., Protat, A. and Machado, L. A. T.: Convective cloud vertical velocity and mass-flux characteristics from radar wind profiler observations during GoAmazon2014/5, J. Geophys. Res. Atmos., 121, 891–913, doi:10.1002/2016JD025303, 2016.

Gonçalves, W. A., Machado, L. A. T., and Kirstetter, P.-E.: Influence of biomass aerosol on precipitation over the Central Amazon: an observational study, Atmos. Chem. Phys., 15, 6789-6800, https://doi.org/10.5194/acp-15-6789-2015, 2015.

Gorgucci, E., Scarchilli, G., and Chandrasekar, V.: A procedure to calibrate multiparameter weather radar using properties of the rain medium, IEEE T. Geosci. Remote, 37, 269–276, 1999.

Greco, S., Scala, J., Halverson, J., Massie, H. L., Jr., Tao-K, W., and Garstang, M.: Amazon coastal squall lines. Part II: Heat and moisture transports, Monthly Weather Review, 122, 623-635, 1994.

Greco, S., Swap, R., Garstang, M., Ulanski, S., Shipham, M., Harriss, R. C., Talbot, R., Andreae, M. O., and Artaxo, P.: Rainfall and surface kinematic conditions over central Amazonia during ABLE 2B, J. Geophys. Res., 95, 1-14, 1990.

Harriss, R. C., Garstang, M., Wofsy, S. C., Beck, S. M., Bendura, R. J., Coelho, J. R. B., Drewry, J. W., Hoell, J. M., Matson, Jr., P. A., McNeal, R. J., Molion, L. C. B., Navarro, R. L., Rabine, V., and Snell, R. L.: The Amazon Boundary Layer Experiment: Wet season 1987, J. Geophys. Res., 95, 721-736, 1990.

Harriss, R. C., Wofsy, S. C., Garstang, M., Browell, E. V., Molion, L. C. B., McNeal, R. J., Hoell, J. M., Bendura, R. J., Beck, S. M., Navarro, R. L., Riley, J. T., Snell, R. L.: The Amazon Boundary Layer Experiment (ABLE-2A): Dry season 1985, J. Geophys. Res., 93, 1351–1360, 1988.

Horel, J., Hahmann, A., and Geisler, J.: An investigation of the annual cycle of the convective activity over the tropical Americas, Journal of Climate, 2, 1388–1403, 1989.

Hubbert, J. and Bringi, V.N.: An iterative filtering technique for the analysis of copolar differential phase and dual-frequency radar measurements, J. Atmos. Oceanic Technol., 12, 643-648, 1995.

Jäkel, E., Wendisch, M., Krisna, T. C., Ewald, F., Kölling, T., Jurkat, T., Voigt, C., Cecchini, M. A., Machado, L. A. T., Afchine, A., Costa, A., Krämer, M., Andreae, M. O., Pöschl, U., Rosenfeld, D., and Yuan, T.: Vertical distribution of the particle phase in tropical deep convective clouds as derived from cloud-side reflected solar radiation measurements, Atmos. Chem. Phys., 17, 9049-9066, https://doi.org/10.5194/acp-17-9049-2017, 2017.

Jarvis, A., Reuter, H.I., Nelson, A., and Guevara, E.: Hole-filled SRTM for the globe Version 4, available from the CGIAR-CSI SRTM 90m Database, “available at: http://srtm.csi.cgiar.org”, 2008.

Koren, I., Altaratz, O., Remer, L. A., Feingold, G., Martins, J. V., and Heiblum, R. H.: Aerosol-induced intensification of rain from the tropics to the mid-latitudes, Nat. Geosci., 5, 118–122, doi:10.1038/ngeo1364., 2012.

Kousky, V. E., and Gan, M. A.: Upper tropospheric cyclonic vortices in the tropical South Atlantic, Tellus, 33, 538-551, 1981.

Lance, S., Brock, C. A., Rogers, D., Gordon, J. A.: Water droplet calibration of the Cloud Droplet Probe (CDP) and inflight performance in liquid, ice and mixed-phase clouds during ARCPAC, Atmos. Meas. Tech., 3, 1683-1706, doi:10.5194/amt-3-1683-2010, 2010.

Laurent, H., Machado, L. A. T., Morales, C. A., and Durieux, L.: Characteristics of the Amazonian mesoscale convective systems observed from satellite and radar during the WETAMC/LBA experiment, J. Geophys. Res., 107, doi:10.1029/2001JD000337, 2002.

Lin, C. Y., Chen, W. C., Chang, P. L., and Sheng, Y. F.: Impact of the urban heat island effect on precipitation over a complex geographic environment in northern Taiwan, Journal of Applied Meteorology and Climatology, 50, 339-353, 2010.

Löffler-Mang, M., Joss, J.: An optical disdrometer for measuring size and velocity of hydrometeors, J. Atmos. Ocean. Technol. 17 , 130–139, 2000.

Machado L. A. T, and Coauthors: The CHUVA Project – how does convection vary across Brazil?, Bull. Amer. Meteor. Soc., 95, 1–10, doi: 10.1175/BAMS-D-13-00084.1, 2014.

Machado, L. A. T., Desbois, M., Duvel, J. P.: Structural Characteristics of Deep Convective Systems over Tropical Africa and the Atlantic Ocean, Monthly Weather Review, 120, 392-406, 1992.

Machado, L. A. T., Laurent, H., and Lima, A. A.: Diurnal march of the convection observed during TRMM-WETAMC/LBA, Journal of Geophysical Research, 107, doi:10.1029/2001JD000338, 2002.

Machado, L. A. T., Rossow, W., Guedes, R. L., and Walker, A.: Life cycle variations of mesoescale convective systems over the Americas, Monthly Weather Review, 126, 1630–1654, 1998.

Machado, L. A. T.,H. Laurent, N. Dessay and I. Miranda.: Seasonal and diurnal variability of convection over the Amazonia: A comparison of different vegetation types and large scale forcing, Theoretical and Applied Climatology, 78, doi:10.1007/s00704-004-0043-x, 2004.

Mallaun, C., Giez, A., and Baumann, R.: Calibration of 3-D wind measurements on a single-engine research aircraft, Atmos. Meas. Tech., 8(8), 3177–3196, doi:10.5194/amt-8-3177-2015, 2015.

Marengo, J. A., Borma, L. S., Rodriguez, D. A., Pinho, P., Soares, W. R., and Alves, L. M.: Recent Extremes of Drought and Flooding in Amazonia: Vulnerabilities and Human Adaptation, American Journal of Climate Change, 02, 87-96, 2013.

Marengo, J., Cornejo, A., Satymurty, P., Nobre, C., and Sea, W.: Cold surges in tropical and extratropical South America: The strong event in June 1994, Monthly Weather Review, 125, 2759–2786, 1997.

Marengo, J.A, Williams, E.R., Alves, L. M, Soares, W. R., Rodrigues, D. A. (Eds.): Exteme seasonal variations in the Amazon Basin: droughts and floods, In Interaction between biosphere, atmosphere and human land use in the Amazon basin. Nagy, L. Forsberg, B. R., Artaxo, P., eds, Springer, 55-76, 2016.

Martin, S. T and Coauthors: The Green Ocean Amazon Experiment (GoAmazon2014/5) Observes Pollution Affecting Gases, Aerosols, Clouds, and Rainfall over the Rain Forest, Bull. Am. Meteorol. Soc., 98, 981-997, doi:10.1175/BAMS-D-15-00221.1, 2017

Martin, S. T., Andreae, M. O., Artaxo, P., Baumgardner, D., Chen, Q., Goldstein, A. H., Guenther, A., Heald, C. L., Mayol-Bracero, O. L., McMurry, P. H., Pauliquevis, T., Pöschl, U., Prather, K. A., Roberts, G. C., Saleska, S. R., Dias, M. A. S., Spracklen, D., Swietlicki, E., and Trebs, I., Sources and properties of Amazonian aerosol particles: Rev. Geophys., 48, RG2002, doi:10.1029/2008RG000280, 2010.

Martin, S. T., Artaxo, P.; Machado, L. A. T.; Manzi, A. O.; Souza, R. A. F.; Schumacher, C.; Wang, J.; Andreae, M. O.; Barbosa, H. M. J.; Fan, J.; Fisch, G.; Goldstein, A. H.; Guenther, A.; Jimenez, J. L.; Poschl, U.; Silva Dias, M. A.; Smith, J. N.; and Wendisch, M.: Introduction: Observations and Modeling of the Green Ocean Amazon (GoAmazon2014/5), Atmospheric Chemistry and Physics (Online), 16, 4785-4797, 2016.

Mattos, E. V., Machado, L. A. T. , Williams, E. R. , Goodman, S. J. , Blakeslee, R. J. , Bailey, J.: Electrification Life Cycle of Incipient Thunderstorms. Journal of Geophysical Research: Atmospheres, 122, 4670-4697, 2017.

Molleker, S., Borrmann, S., Schlager, H., Luo, B., Frey, W., Klingebiel, M., Weigel, R., Ebert, M., Mitev, V., Matthey, R., Woiwode, W., Oelhaf, H., Dörnbrack, A., Stratmann, G., Grooß, J.-U., Gün-ther, G., Vogel, B., Müller, R., Krämer, M., Meyer, J., and Cairo, F.: Microphysical properties of syn-optic scale polar stratospheric clouds: in situ measurements of unexpectedly large HNO3 containing particles in the Arctic vortex, Atmos. Chem. Phys., 14, 10785-10801, doi:10.5194/acp-14-10785-2014, 2014.

Negri, A. J., Anagnostou, E. N., and Adler, R. F.: A 10-yr climatology of Amazonian rainfall derived from passive microwave satellite observations, J. Appl. Meteor., 39, 42–56, doi:10.1175/1520-0450(2000)039,0042:AYCOAR.2.0.CO;2, 2000.

Petersen, W.A., and Rutledge, S.A.: Regional Variability in Tropical Convection: Observations from TRMM, J. Climate, 14, 3566-3585, 2001.

Pöhlker, M. L., Pöhlker, C., Klimach, T., Hrabe de Angelis, I., Barbosa, H. M. J., Brito, J., Carbone, S., Cheng, Y., Chi, X., Ditas, F., Ditz, R., Gunthe, S. S., Kesselmeier, J., Könemann, T., Lavrič, J. V., Martin, S. T., Moran-Zuloaga, D., Rose, D., Saturno, J., Su, H., Thalman, R., Walter, D., Wang, J., Wolff, S., Artaxo, P., Andreae, M. O., and Pöschl, U.: Long-term observations of cloud condensation nuclei in the Amazon rain forest – Part 1: Aerosol size distribution, hygroscopicity, and new model parameterizations for CCN prediction, Atmos. Chem. Phys., 16, 15709-15740, 10.5194/acp-2016-519, 2016

Rickenbach, T. M.: Nocturnal cloud systems and the diurnal variation of clouds and rainfall in southwestern Amazonia, Mon.Wea. Rev., 132, 1201–1219, doi:10.1175/1520-0493(2004)132,1201, 2004.

Rickenbach, T., Ferreira, R. N., Halverson, J., and Silva Dias, M. A. F.: Modulation of convection in the southwestern Amazon basin by extratropical stationary fronts, J. Geophys. Res., 107, doi:10.1029/2000JD000263, 2002.

Roberts, G. C., Andreae, M. O., Zhou, J., and Artaxo, P.: Cloud condensation nuclei in the Amazon Basin: "Marine" conditions over a continent?, Geophys. Res. Lett., 28, 2807-2810, 2001.

Rose, D., Gunthe, S. S., Mikhailov, E., Frank, G. P., Dusek, U., Andreae, M. O., and Poeschl, U.: Calibration and measurement uncertainties of a continuous-flow cloud condensation nuclei counter (DMT-CCNC): CCN activation of ammonium sulfate and sodium chloride aerosol particles in theory and experiment, Atmospheric Chemistry and Physics, 8, 1153-1179, 2008

Rosenfeld D. and Ulbrich, C. W. (Eds.): Cloud microphysical properties, processes, and rainfall estimation opportunities, Chapter 10 of " Radar and Atmospheric Science: A Collection of Essays in Honor of David Atlas", Edited by Roger M. Wakimoto and Ramesh Srivastava, Meteorological Monographs 52, 237-258, AMS, 2003.

Rosenfeld, D.: Flood or drought: How do aerosols affect precipitation?, Science, 321, 1309–1313, 2008.

Saad, S. I., da Rocha, H. R., Silva Dias, M. A. F., and Rosolem, R.: Can the Deforestation Breeze Change the Rainfall in Amazonia? A Case Study for the BR-163 Highway Region, Earth Interactions, 14, 1-25, 2010.

Santos, M. J., Silva Dias, M.A. F., and Freitas, E. D.: Influence of local circulations on wind moisture and precipitation close to Manaus City, Amazon Region – Brazil, Journal of Geophysical Research, 119, 233-249, doi:10.1002/2014JD021969, 2014.

Saraiva, I., Silva Dias, M. A. F., Morales, C. A. R., and Saraiva, J. M. B.: Regional variability of rainclouds in the Amazon basin seen by a network of weather radars, Journal of Applied Meteorology and Climatology, https://doi.org/10.1175/JAMC-D-15-0183.1, 2016.

Schneebeli, M. , Sakuragi, J. , Biscaro, T. S. , Angelis, C. F. , Costa, I. C. , Morales, C. , Baldini, L. , Machado, L. A. T.: Polarimetric X-band weather radar measurements in the tropics: radome and rain attenuation correction, Atmospheric Measurement Techniques, 5, 2183-2199, 2012.

Shilling, J. E., Pekour, M. S., Fortner, E. C., Artaxo, P., de Sá, S., Hubbe, J. M., Longo, K. M., Machado, L. A. T., Martin, S. T., Springston, S. R., Tomlinson, J., and Wang, J.: Aircraft Observations of Aerosol in the Manaus Urban Plume and Surrounding Tropical Forest during GoAmazon 2014/15, Atmos. Chem. Phys. Discuss., https://doi.org/10.5194/acp-2018-193, in review, 2018.

Silva Dias, M. A. F., Silva Dias, P. L., Longo, M., Fitzjarrald, D. R., and Denning, A. S.: River breeze circulation in Eastern Amazon: observations and modeling results, Theoretical and Applied Climatology, 78, 111-121, 2004.

Silva Dias, M.A. F., and Carvalho, L. M. V. (Eds.): The South American Monsoon System. In: The Global Monsoon System Research and Forecast (3rd Edition) C. P. Chang Ed., World Scientific Publishing Co., Chapter 3. (in press), 2016.

Silva Dias, M.A.F., Rutledge, S., Kabat, P., Silva Dias , P. L., Nobre, C. A., Fisch, G., Dolman, A J, Zipser, E., Garstang, M., Manzi, A. O., Fuentes, J., Rocha, H. R., Marengo, Jose, Plana-Fattori, A., Sá, L., Alvalá, R., Andreae, M., Artaxo, Paulo, Gielow, R., and Gatti, L.: Clouds and rain processes in a biosphere atmosphere interaction context in the Amazon Region, Journal of Geophysical Research., 107, 46.1 - 46.23, 2002.

Silva Dias, P. L., Schubert, W. H., and DeMaria, M.: Large-scale response of the tropical atmosphere to transient forcing, J. Atmos. Sci., 40, 2689-2707, 1983.

Siqueira, J. R., and Machado, L. A. T.: Influence of frontal systems on the day-to-day convection variability over South America, J. Climate, 17, 1754–1766, 2004.

Souza, D. O. and Alvalá, R. C. S.: Observational evidence of the urban heat island of Manaus City, Brazil, Met. Apps., 21, 186–193, doi:10.1002/met.1340, 2014.

Tanaka, L., Satiamurty, P., and Machado, L. A. T.: Diurnal variation of precipitation in central Amazon Basin, International Journal of Climatology, 34, 2014.

Testud, J., Bouar, E. L., Obligis, E., and Ali-Mehenni, M.: The rain-profiling algorithm applied to polarimetric weather radar data, J. Atmos. Ocean. Tech., 17, 332–356, 2000.

Thalman, R., de Sá, S. S., Palm, B. B., Barbosa, H. M. J., Pöhlker, M. L., Alexander, M. L., Brito, J., Carbone, S., Castillo, P., Day, D. A., Kuang, C., Manzi, A., Ng, N. L., Sedlacek III, A. J., Souza, R., Springston, S., Watson, T., Pöhlker, C., Pöschl, U., Andreae, M. O., Artaxo, P., Jimenez, J. L., Martin, S. T., and Wang, J.: CCN activity and organic hygroscopicity of aerosols downwind of an urban region in central Amazonia: seasonal and diel variations and impact of anthropogenic emissions, Atmos. Chem. Phys., 17, 11779-11801, https://doi.org/10.5194/acp-17-11779-2017, 2017.

Tokay, A., and Short, D. A.: Evidence from tropical raindrop spectra of the origin of rain from stratiform versus convective clouds, J. Appl. Meteor., 35, 355–371, 1996.

Tokay, A., Petersen, W.A., Gatlin, P., and Wingo, M.: Comparison of raindrop size distribution measurements by collocated disdrometers, J. Atmos. Ocean. Technol., 30, 1672–1690, 2013.

Vila, D. A., Machado L. A. T., Laurent H., and Velasco, I.: Forecast and Tracking the Evolution of Cloud Clusters (ForTraCC) using satellite infrared imagery: Methodology and validation, Wea. Forecasting, 23, 233-245, doi: 10.1175/2007WAF2006121.1, 2008.

Wang, D., Giangrande, S. E., Bartholomew, M. J., Hardin, J., Feng, Z., Thalman, R., and Machado, L. A.: The Green Ocean: Precipitation Insights from the GoAmazon2014/5 Experiment, Atmos. Chem. Phys. Discuss., https://doi.org/10.5194/acp-2018-101, in review, 2018.

Wang, J., Krejci, R., Giangrandel, S., Kuang, C., Barbosa, H. M. J., Brito, J., Carbone, S., Chi, X. G., Comstock, J., Ditas, F., Lavric, J., Manninen, H. E., Mei, F., Moran-Zuloaga, D., Pohlker, C., Pohlker, M. L., Saturno, J., Schmid, B., Souza, R. A. F., Springston, S. R., Tomlinson, J. M., Toto, T., Walter, D., Wimmer, D., Smith, J. N., Kulmala, M., Machado, L. A. T., Artaxo, P., Andreae, M. O., Petaja, T., and Martin, S. T.: Amazon boundary layer aerosol concentration sustained by vertical transport during rainfall, Nature, 539, 416–419, 2016.

Weigel, R., Spichtinger, P., Mahnke, C., Klingebiel, M., Afchine, A., Petzold, A., Krämer, M., Costa, A., Molleker, S., Reutter, P., Szakáll, M., Port, M., Grulich, L., Jurkat, T., Minikin, A., and Borrmann, S.: Thermodynamic correction of particle concentrations measured by underwing probes on fast-flying aircraft, Atmos. Meas. Tech., 9, 5135-5162, doi:10.5194/amt-9-5135-2016, 2016.

Wendisch, M., and Brenguier, J. L. (Eds.): Airborne Measurements for Environmental Research: Methods and Instruments. Wiley-VCH Verlag GmbH & Co. KGaA, Weinheim, Germany. ISBN: 978-3-527-40996-9, doi:10.1002/9783527653218, 2013.

Wendisch, M., et al: The ACRIDICON-CHUVA campaign: Studying tropical deep convective clouds and pre-cipitation over Amazonia using the new German research aircraft HALO. Bull. Am. Meteorol. Soc., 97, 10, 1885-1908, http://dx.doi.org/10.1175/BAMS-D-14-00255.1, 2016.

Williams, E., and Coauthors: Contrasting convective regimes over the Amazon: Implications for cloud electrification, J. Geo- phys. Res., 107, doi:10.1029/2001JD000380, 2002

Zhuang, Y., Fu, R., Marengo, J. A., and Wang, H.: Seasonal variation of shallow-to-deep convection transition and its link to the environmental conditions over the Central Amazon, J. Geophys. Res. Atmos., 122, https://doi.org/10.1002/2016JD025993, 2017.

.

## Figure captions

**Figure 1:** Rainfall rate (RR) histogram for wet and dry seasons computed using the T3 disdrometer. Wet and dry seasons occurred from January to March and August to October, respectively, for the years 2014 and 2015. Rainfall rate (RR) and total rainfall (R) are given in the legend

**Figure 2:** Box Plots illustrating monthly a) convective available potential energy (CAPE), b) convective inhibition energy (CINE), c) precipitable water vapour (PWV), d) lifting condensation level (LCL), e) bulk shear and f) mean rainfall rate (RR) and rainfall. Data are for 2014 and were collected at 00, 06, 12 and 18 UTC using the T3 radiosondes. Rainfall was computed using the T3 rain gauge. Each box represents the 25% to 75% populations and the line inside the box shows the median value; circles represent outliers.

**Figure 3:** Rain cell (left, based on the SIPAM S-band radar) and cloud cluster (right, based on GOES-13 IR brightness temperature [$B_T$]) size distributions between wet and dry seasons; and the difference between dry and wet season distributions (in black, right axis)

**Figure 4:** Mass-weighted mean raindrop diameter ($D_m$) as a function of the rainfall rate (RR) for wet and dry seasons for a) convective and b) stratiform rain events. The arrows on the x-axis indicate variations in the averages based on the Student's t-test (95% confidence). The box represents the 25% to 75% populations and the line inside the box shows the median value; the circles are the outliers.

**Figure 5:** X-band radar reflectivity contoured frequency by altitude diagram (CFAD) for the wet (top) and dry (bottom) seasons. Each CFAD consists of a PDF of reflectivity (2 dBZ bin intervals) at each height (400 m bin intervals) multiplied by 100 so that values are displayed as a percentage.

**Figure 6:**

ZDR (gives an idea of horizontal–positively and vertical–negatively oriented hydrometeors), KDP (gives an idea of hydrometeor concentration and hydrometeor orientation) and horizontal-vertical correlation (gives an idea of the homogeneity of the hydrometeor) contoured frequency by altitude diagram (CFAD) for the wet (top) and dry (bottom) seasons as derived using the X-band radar. Each CFAD consists of a PDF of ZDR (0.5 dB bin intervals), KDP (0.5 dB bin intervals) and co-polar correlation (0.05 bin intervals) at each height (400 m bin intervals) multiplied by 100 so that the values are displayed as a percentage.

**Figure 7:** Mass-weighted mean rainfall diameter as a function of the rainfall rate (RR) during the wet season for clean (CPC smaller than the 33$^{rd}$ percentile) and polluted (CPC larger than the 66$^{th}$ percentile) air over pasture. Each box represents the 25% to 75% populations, and the line inside the box shows the median value; circles represent outliers.

**Figure 8:** a) Four vegetation classes, as obtained from the digital Terra-Class classification: forest, hydrography, non-forest, and urban area; and b) Topography across a 150 km radius as derived using SIPAM radar. X-band (T3 site) and S-band radar positions are shown in the figure.

**Figure 9:** Rainfall rate (RR; from S-band radar) box plots for the wet and dry seasons given different surface cover classes. Each box represents the 25% to 75% populations, and the line inside the box represents the median value.

**Figure 10:** AC17 flight paths over forested and deforested regions. Flight legs 1 and 2 are shown in red on panels (A) and (C), respectively (source from Google Earth). The dot on the flight leg 1 corresponds to 56°57'W, 4°13'S and that on flight leg 2 corresponds to 55°17'W, 5°53´S. Visible GOES-13 images for flight legs 1 and 2 at the time of each flight are shown on panels (B) and (C), respectively.

**Figure 11:** a) Cloud droplet concentration as a function of liquid water content; b) mass-weighted mean cloud diameter as a function of vertical velocity; and c) cloud droplet concentration as a function of vertical velocity for forest and pasture at different heights.

**Figure 12:** CCN concentration ($N_{CCN}$) cumulative histogram for (a) leg 1 and (b) leg 2 of AC17 flight paths over forested and non-forested regions at different flight heights.

**Figure 13:** Wet and dry season rainfall rate (RR) box plots for different topography classes. Each box represents the 25% to 75% populations, and the line inside the box represents the median value. The line represents the remaining population.

**Figures**

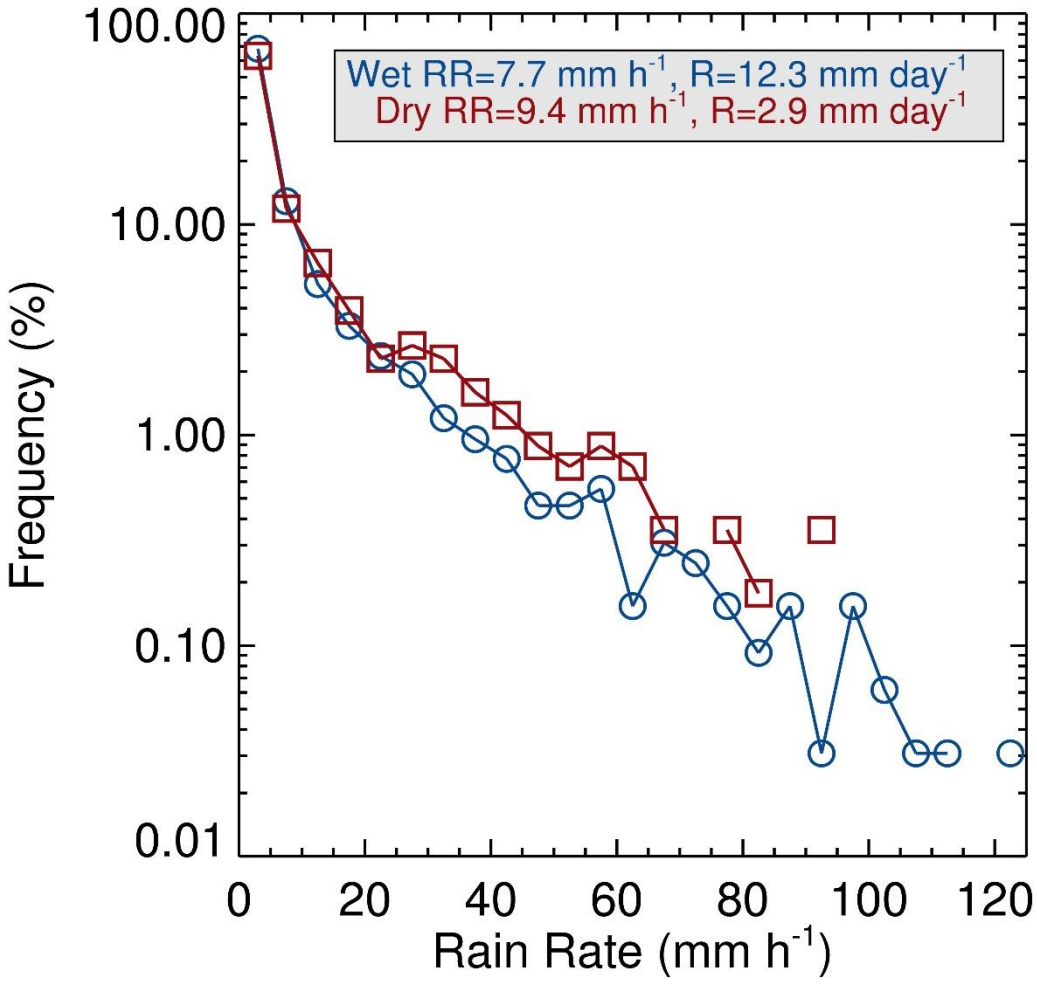


Figure 1. Rainfall rate (RR) histogram for wet and dry seasons computed using the T3 disdrometer. Wet and dry seasons occurred from January to March and August to October, respectively, for the years 2014 and 2015. Rainfall rate (RR) and total rainfall (R) are given in the legend.

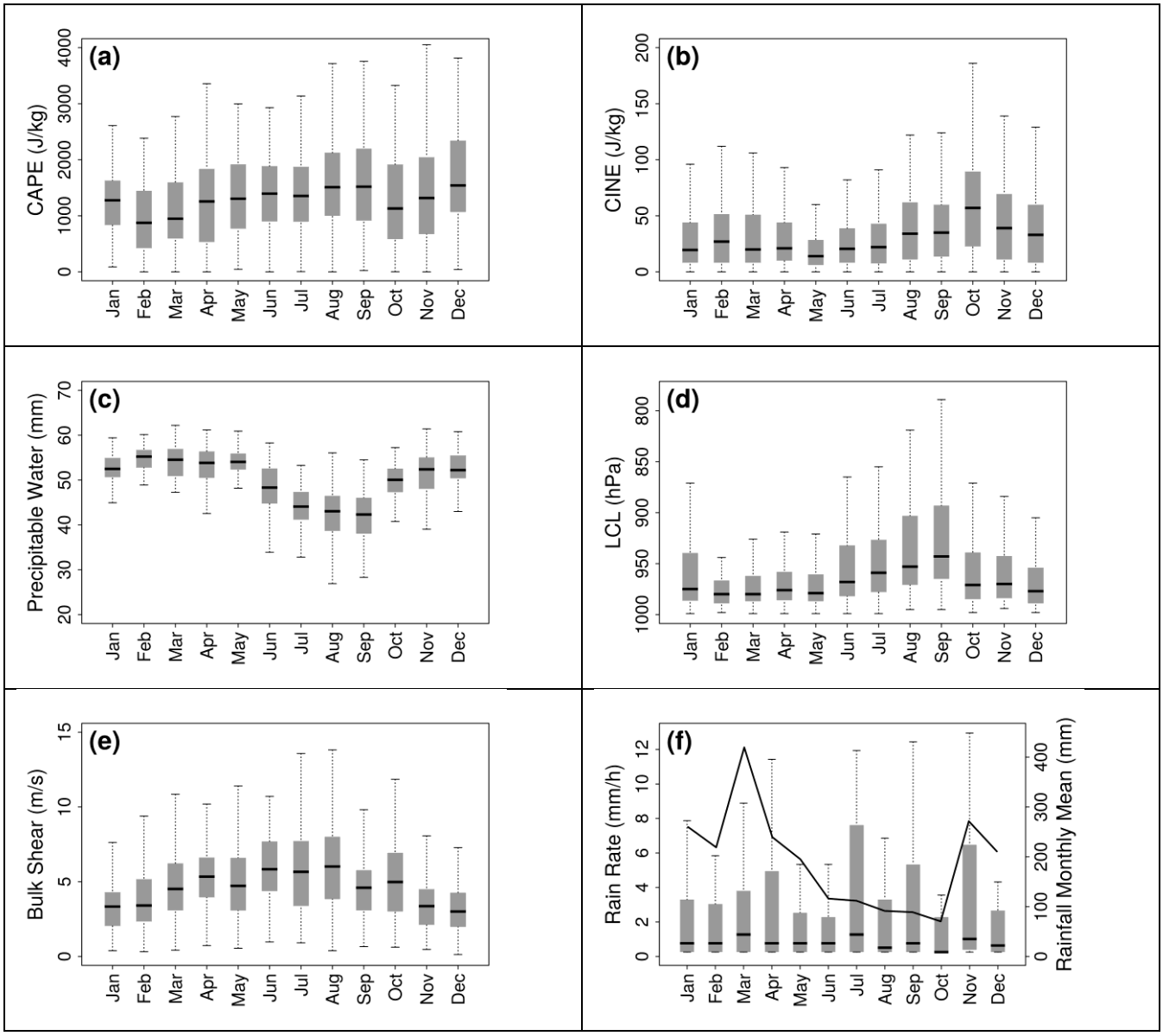


**Figure 2:** Box Plots illustrating monthly a) convective available potential energy (CAPE), b) convective inhibition energy (CINE), c) precipitable water vapour (PWV), d) lifting condensation level (LCL), e) bulk shear and f) mean rainfall rate (RR) and rainfall. Data are for 2014 and were collected at 00, 06, 12 and 18 UTC using the T3 radiosondes. Rainfall was computed using the T3 rain gauge. Each box represents the 25% to 75% populations and the line inside the box shows the median value; circles represent outliers.

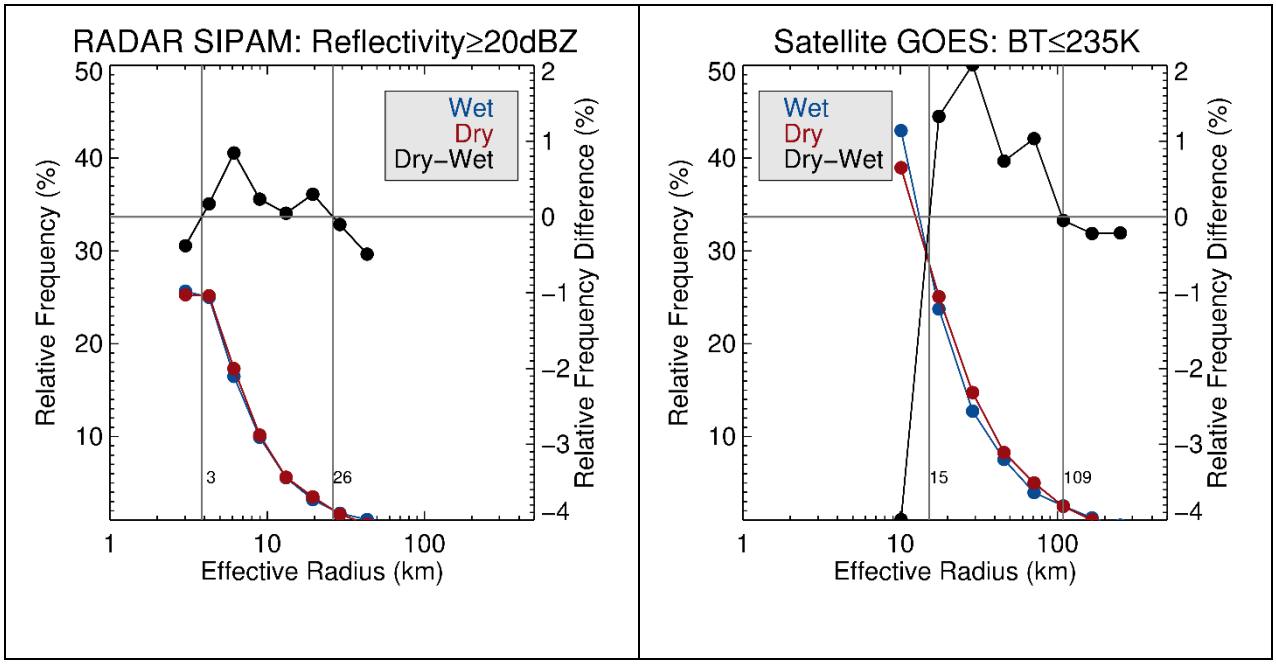


Figure 3: Rain cell (left, based on the SIPAM S-band radar) and cloud cluster (right, based on GOES-13 IR brightness temperature [$B_T$]) size distributions during the wet and dry seasons; and the difference between the dry and wet season distributions (in black, right axis)

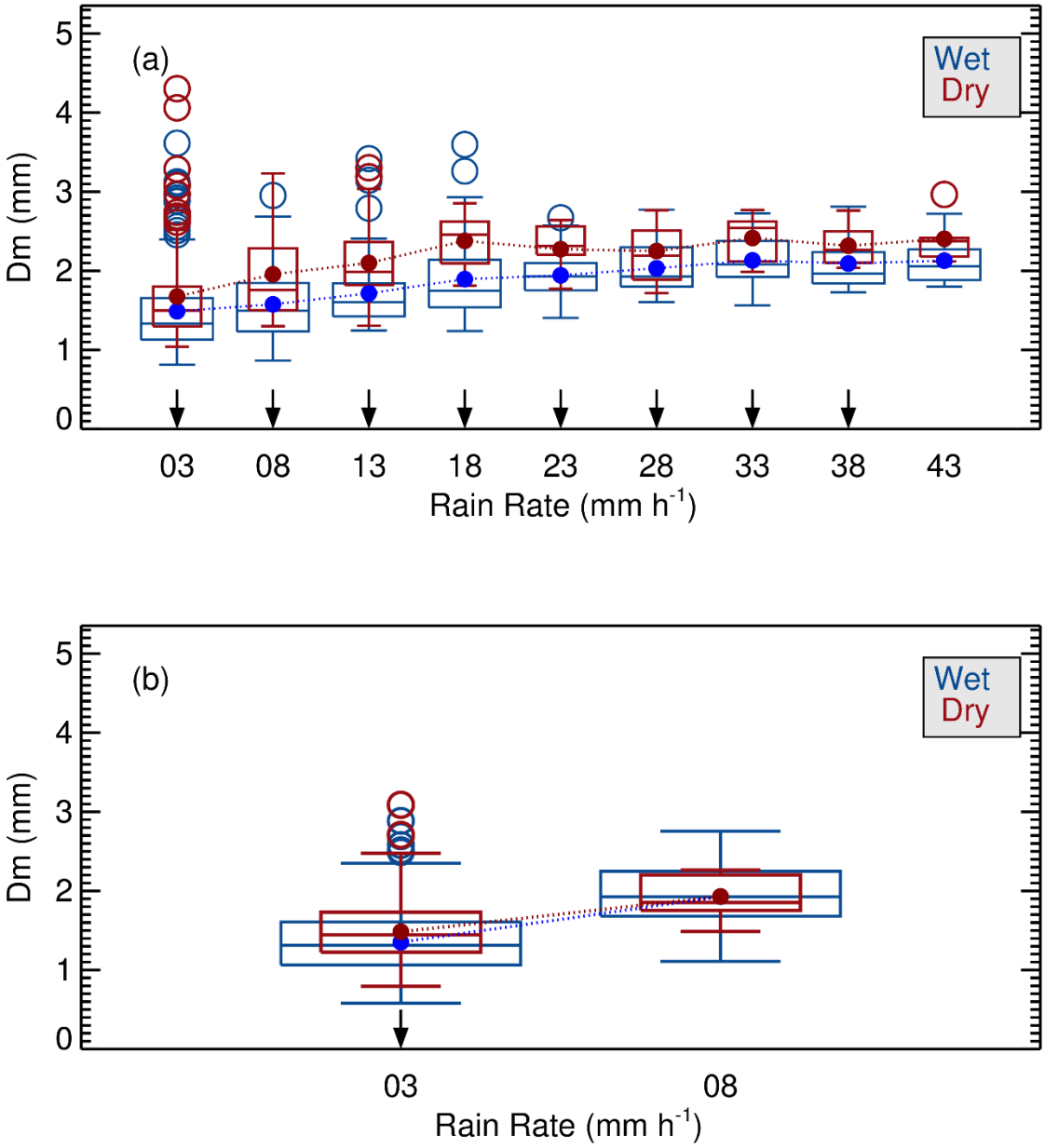


Figure 4: Mass-weighted mean raindrop diameter ($D_m$) as a function of the rainfall rate (RR) for wet and dry seasons for a) convective and b) stratiform rain events. The arrows on the x-axis indicate variations in the averages based on the Student's t-test (95% confidence). The box represents the 25% to 75% populations and the line inside the box shows the median value; the circles are the outliers.

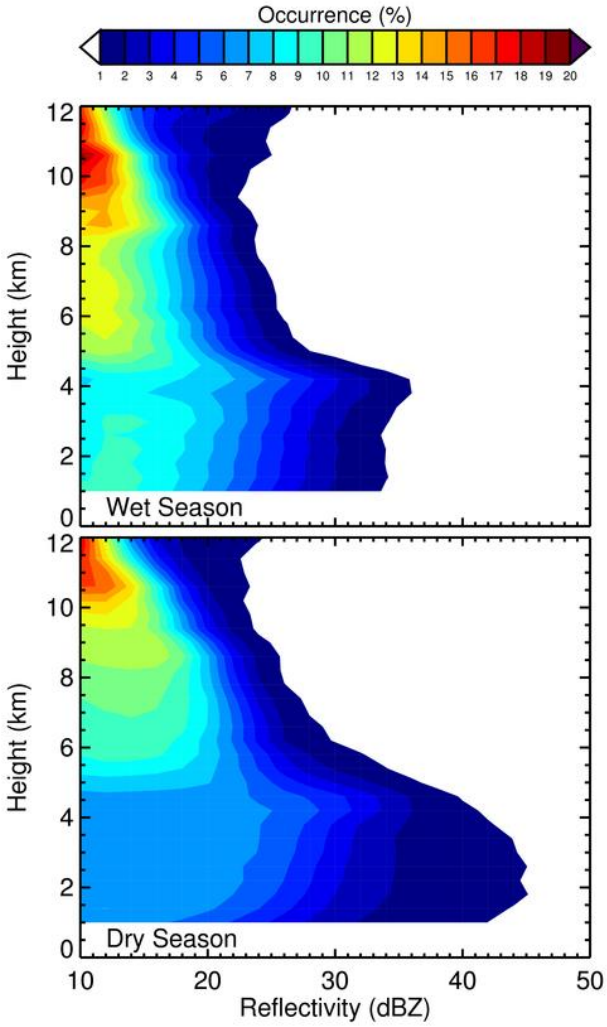


Figure 5: X-band radar reflectivity contoured frequency by altitude diagram (CFAD) for the wet (top) and dry (bottom) seasons. Each CFAD consists of a PDF of reflectivity (2 dBZ bin intervals) at each height (400 m bin intervals) multiplied by 100 so that values are displayed as a percentage.

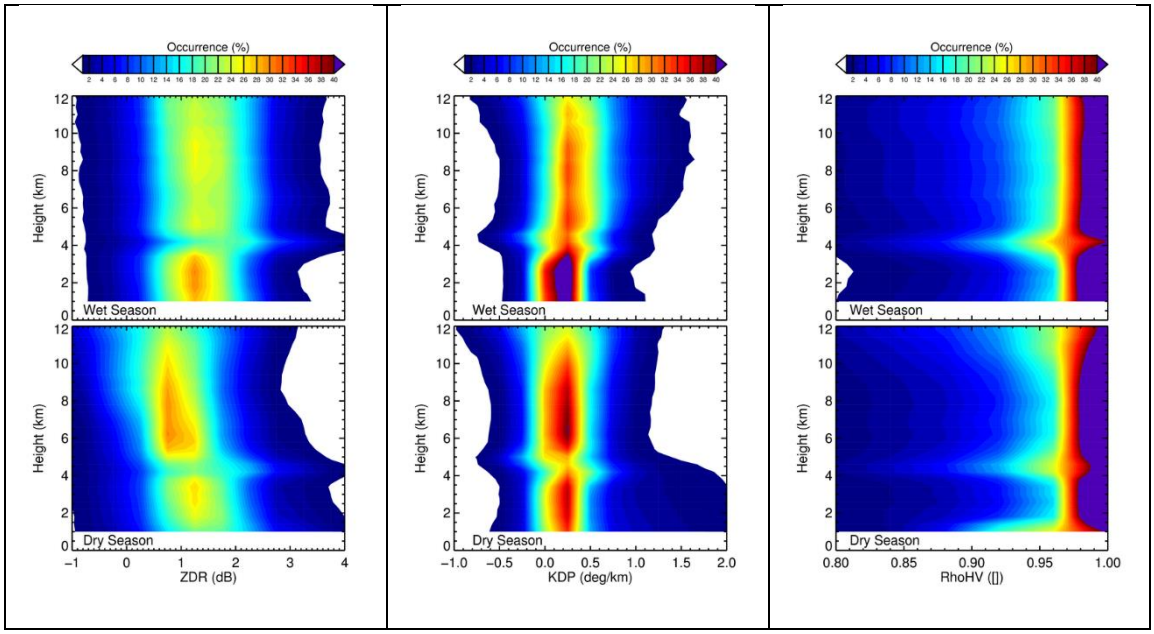


**Figure 6:** ZDR (gives an idea of horizontal–positively and vertical–negatively oriented hydrometeors), KDP (gives an idea of hydrometeor concentration and hydrometeor orientation) and horizontal-vertical correlation (gives an idea of the homogeneity of the hydrometeor) contoured frequency by altitude diagram (CFAD) for the wet (top) and dry (bottom) seasons as derived using the X-band radar. Each CFAD consists of a PDF of ZDR (0.5 dB bin intervals), KDP (0.5 dB bin intervals) and co-polar correlation (0.05 bin intervals) at each height (400 m bin intervals) multiplied by 100 so that the values are displayed as a percentage.

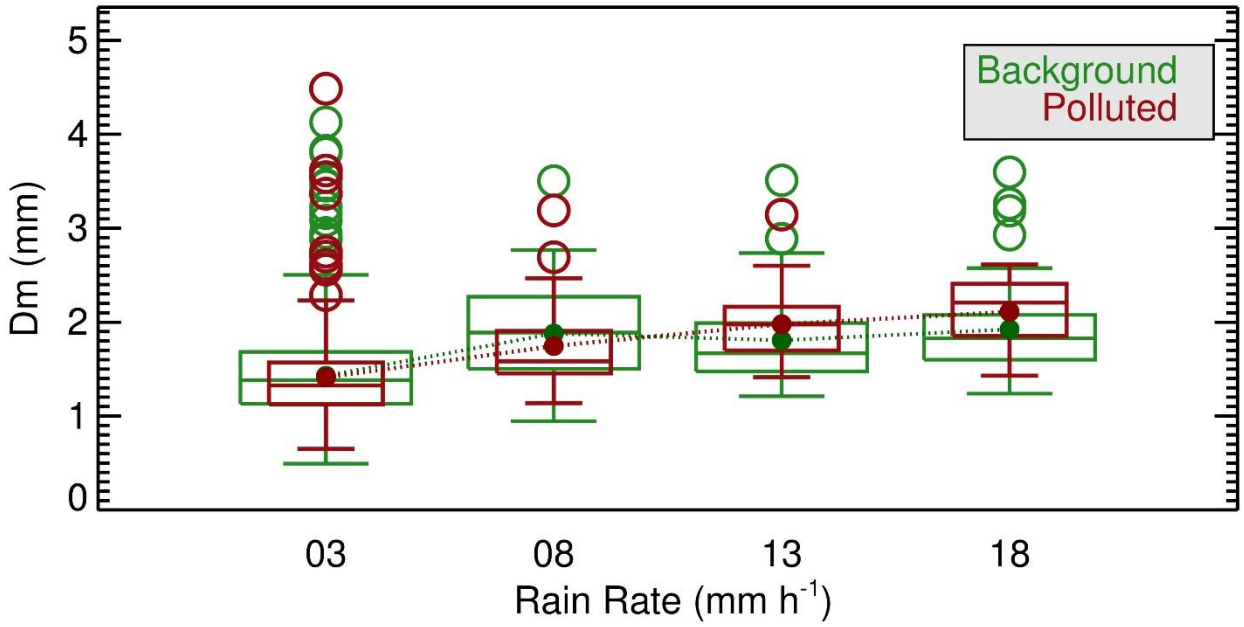


Figure 7: Mass-weighted mean rainfall diameter as a function of the rainfall rate (RR) during the wet season for clean (CPC smaller than the 33rd percentile) and polluted (CPC larger than the 66th percentile) air over pasture. Each box represents the 25% to 75% populations, and the line inside the box shows the median value; circles represent outliers.

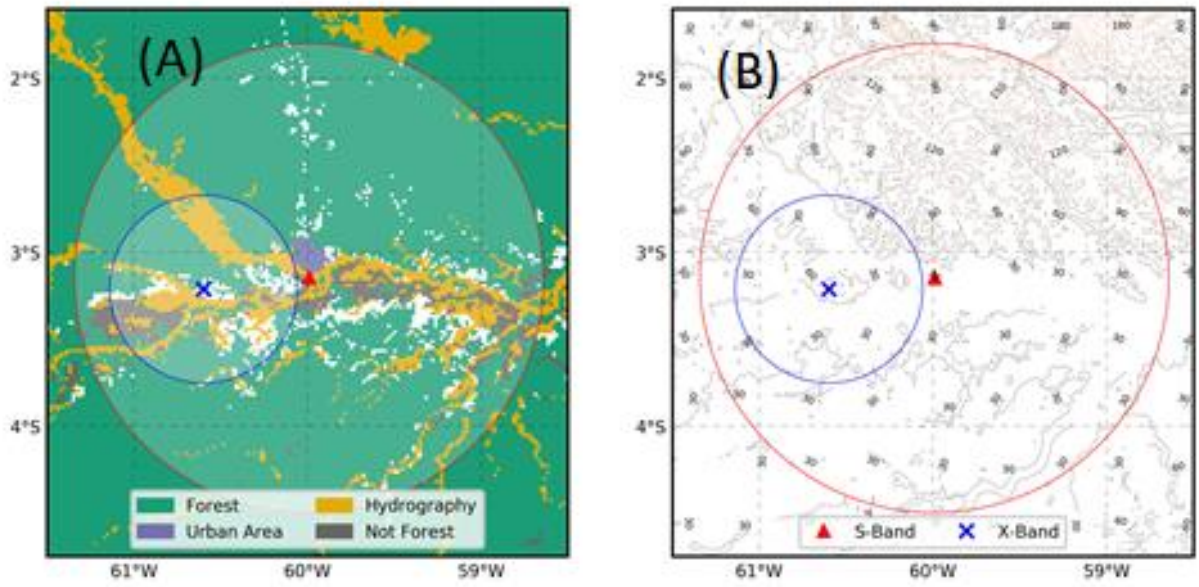


**Figure 8:** a) Four vegetation classes, as obtained from the digital Terra-Class classification: forest, hydrography, non-forest, and urban area; and b) Topography across a 150 km radius as derived using SIPAM radar. X-band (T3 site) and S-band radar positions are shown in the figure.

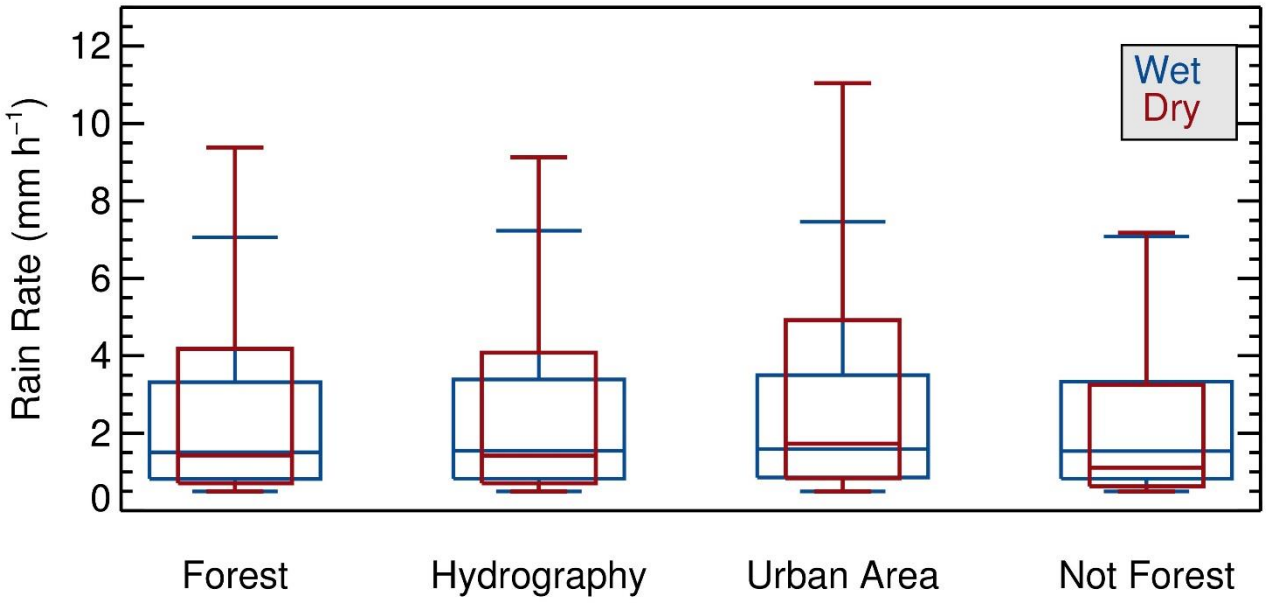


**Figure 9:** Rainfall rate (from S-band radar) box plots for the wet and dry seasons given different surface cover classes. Each box represents the 25% to 75% populations, and the line inside the box represents the median value.

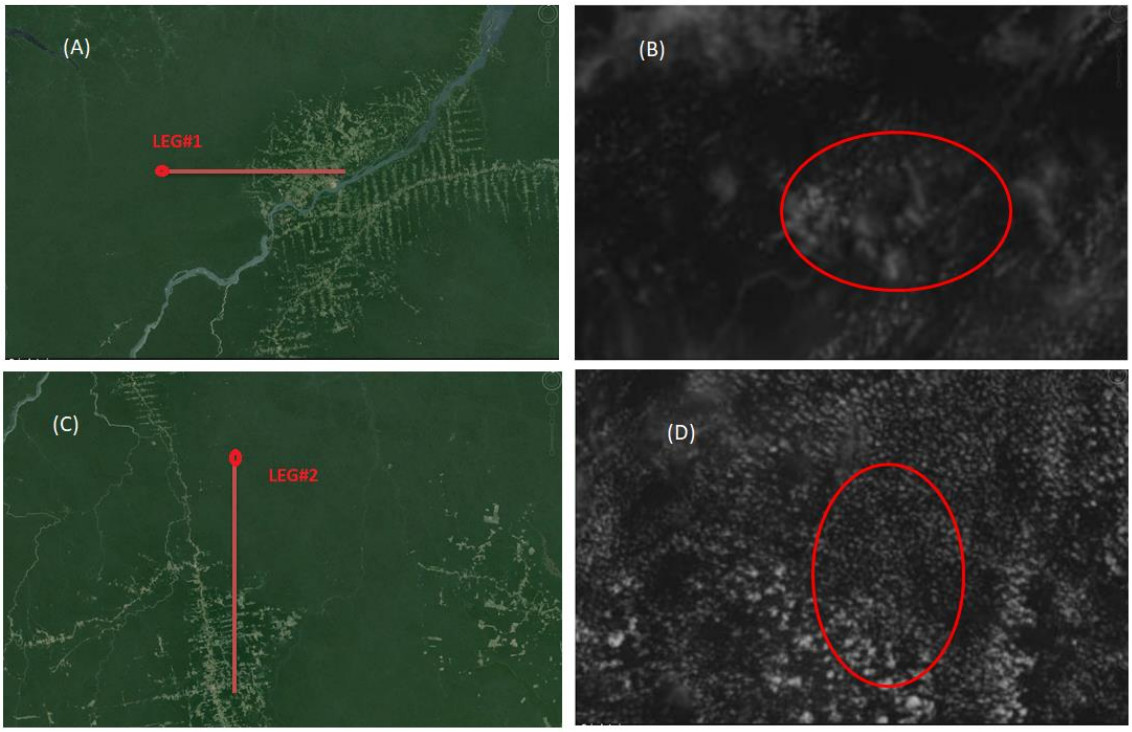


**Figure 10:** AC17 flight paths over forested and deforested regions. Flight legs 1 and 2 are shown in red on panels (A) and (C), respectively (source from Google Earth). The dot on the flight leg 1 corresponds to 56°57'W, 4°13'S and that on flight leg 2 corresponds to 55°17'W, 5°53´S. Visible GOES-13 images for flight legs 1 and 2 at the time of each flight are shown on panels (B) and (C), respectively.

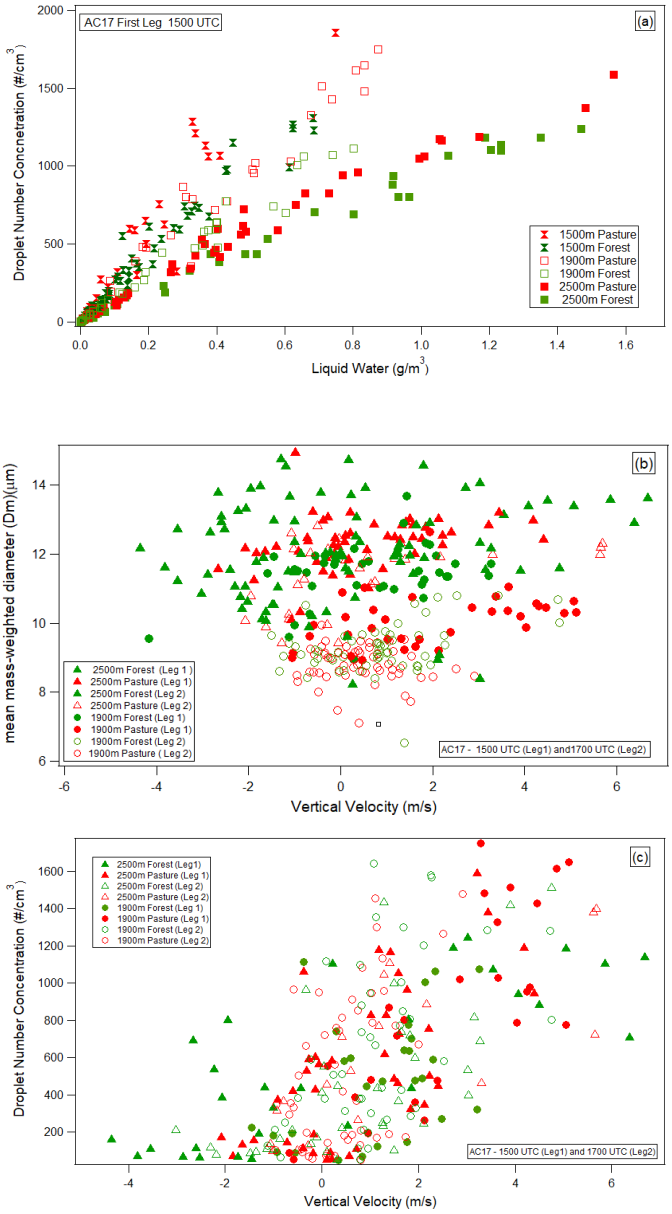


Figure 11: a) Cloud droplet concentration as a function of liquid water content; b) mass-weighted mean cloud diameter as a function of vertical velocity; and c) cloud droplet concentration as a function of vertical velocity for forest and pasture at different heights.

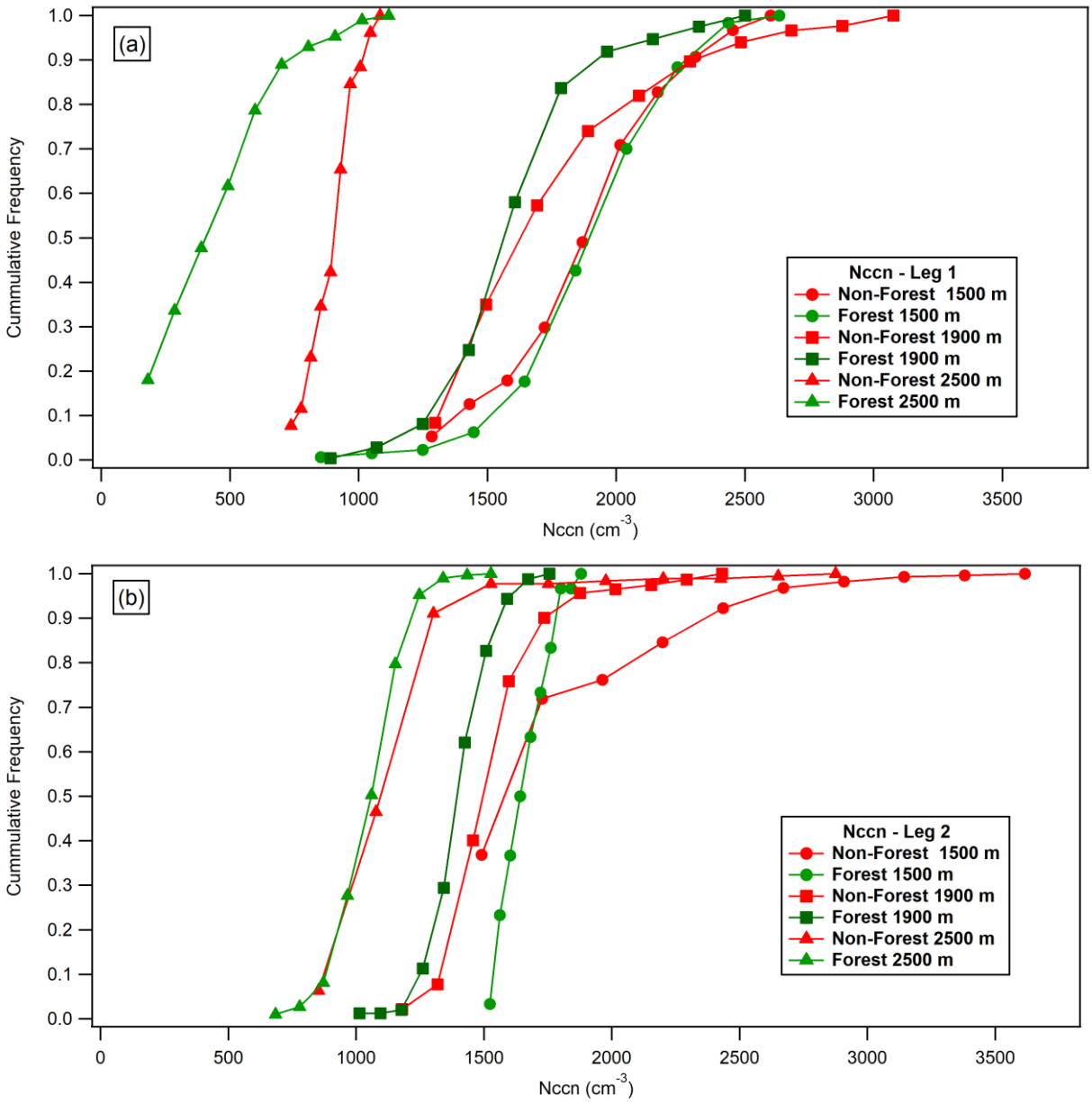


Figure 12: CCN concentration ($N_{CCN}$) cumulative histogram for (a) leg 1 and (b) leg 2 of AC17 flight paths over forested and non-forested regions at different flight heights.

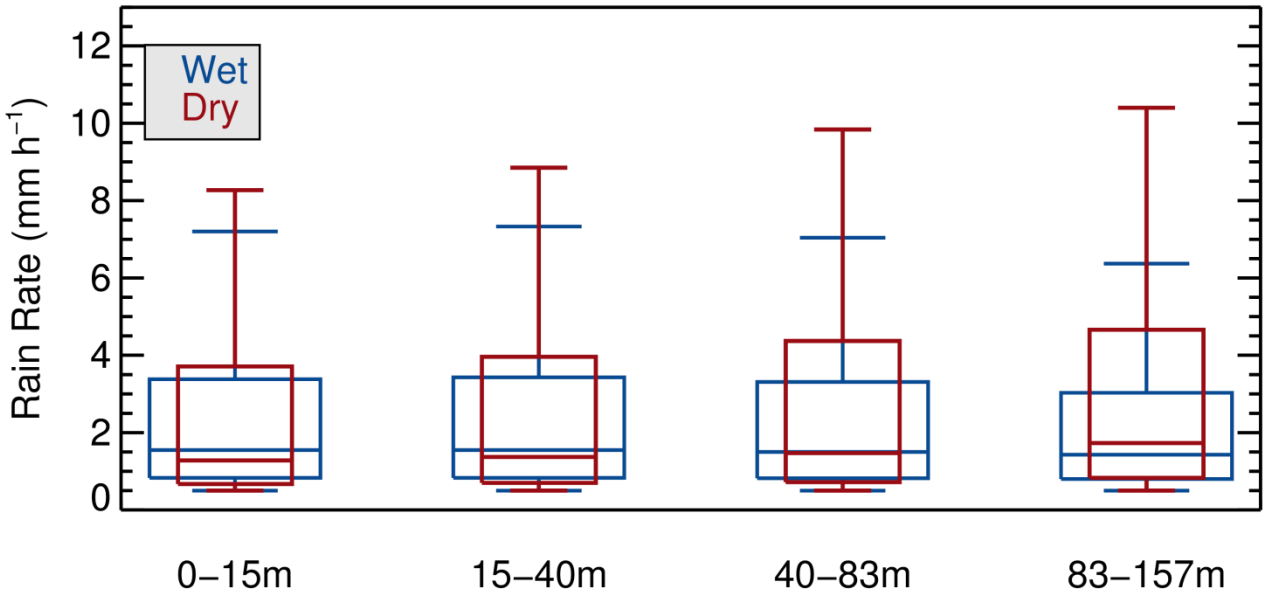


Figure 13: Wet and dry season rainfall rate box plots for different topography classes. Each box represents the 25% to 75% populations, and the line inside the box represents the median value. The line represents the remaining population.